

# Which global reanalysis dataset represents better in snow cover on the Tibetan Plateau?

Shirui Yan<sup>1</sup>, Yang Chen<sup>1</sup>, Yaliang Hou<sup>1</sup>, Kexin Liu<sup>1</sup>, Xuejing Li<sup>1</sup>, Yuxuan Xing<sup>1</sup>, Dongyou Wu<sup>1</sup>,  
5 Jiecan Cui<sup>2</sup>, Yue Zhou<sup>1</sup>, Xin Wang<sup>1, \*</sup>, Wei Pu<sup>1, \*</sup>

<sup>1</sup> Key Laboratory for Semi-Arid Climate Change of the Ministry of Education, College of Atmospheric Sciences, Lanzhou University, Lanzhou 730000, China.

<sup>2</sup> Zhejiang Development & Planning Institute, Hangzhou 310030, China.

10

*Correspondence to:* Wei Pu, ([puwei@lzu.edu.cn](mailto:puwei@lzu.edu.cn)); Xin Wang, ([wxin@lzu.edu.cn](mailto:wxin@lzu.edu.cn))

**Abstract.** The extensive snow cover across the Tibetan Plateau (TP) has a major influence on the climate and water supply for over one billion downstream inhabitants. However, an adequate evaluation of Snow Cover Fraction (SCF) variability over the TP simulated by multiple reanalysis datasets has yet to be undertaken. In this study, we used the Snow Property Inversion from Remote Sensing (SPIReS) SCF dataset from the Water Years (WYs) 2001–2017 to evaluate the capabilities of eight reanalysis datasets (HMASR, MERRA2, ERA5, ERA5L, JRA55, CFSR, CRAL, and GLDAS) in simulating the spatial and temporal variability of SCF in the TP. CFSR, GLDAS, CRAL, and HMASR are well in simulating the spatial pattern of climatological SCF with lower bias and higher correlation and Taylor Skill Score (SS). In contrast, ERA5L, JRA55, and ERA5 has relatively good performance in terms of SCF annual trends among eight reanalysis datasets. The biases in SCF simulations across reanalysis datasets are influenced by a combination of meteorological forcings, including snowfall and temperature, as well as the SCF parameterization methods. However, the primary influencing factors vary among the reanalysis datasets. Additionally, averaging multiple reanalysis datasets can enhance the spatiotemporal accuracy of SCF simulations, but this enhancement effect does not consistently increase with the number of reanalysis datasets used.

### **Keywords**

Snow cover; Tibetan Plateau; Reanalysis dataset; Meteorological forcing factors; Parameterization methods

## 1 Introduction

Widespread snow cover on the Tibetan Plateau (TP), with its high albedo and low thermal conductivity, plays a crucial role in the surface energy balance (Zhang, 2005) and affects the climate locally (Zhang et al., 2022), across Asia, and globally (Lyu et al., 2018; Ma et al., 2017). Furthermore, in its role as the “Asian water tower” (Kitoh and Arakawa, 2016; Qiu, 2008; Xu et al., 2008), the snow that accumulates on the TP during the cold season is an essential freshwater resource for over a billion people during the warm season, supplying their domestic, agricultural, and industrial water needs (Immerzeel et al., 2010). In the context of climate change, the snow cover over the TP is an extremely sensitive element to warming (Yao et al., 2019; You et al., 2020b). Therefore, the accurate and reliable representation of snow cover over the TP is crucial to regional climate and ecosystem studies.

Comprehensive ground-based measurements face challenges due to the complex terrain and harsh weather conditions on the TP (Yang et al., 2019), leading to issues of spatial representativeness. In contrast, optical satellite observations provide global-scale snow cover data and offer crucial support for snow research. For example, NASA’s Moderate Resolution Imaging Spectroradiometer (MODIS) has been providing moderate-resolution global daily snow cover fraction (SCF) data since 2000 (Hall et al., 2002). The Snow Property Inversion from Remote Sensing (SPIReS) then uses a more advanced spectral unmixing technique that provides improvements to SCF estimates for the period Water Years (WYs) 2000–2021 (Bair et al., 2021). However, the more precise satellite products and remote sensing data using more advanced methods have relatively short time spans from 2000 to the present, limiting their role in long-term climate analysis.

Reanalysis methods based on observations and mathematical models (Fujiwara et al., 2017) provide a critical avenue for obtaining long-term snow information. These techniques use data assimilation to integrate historical environmental observations with short-term weather forecasts, yielding optimal estimates of global or regional weather and climate states (Lei et al., 2023). In recent decades, the major meteorological agencies around the world have generated atmospheric and land reanalysis products at varying temporal and spatial resolutions (Fujiwara

60 et al., 2017). Reanalysis datasets have become indispensable sources of data when it comes to  
studying processes related to snow variability, as well as their impacts and responses to climate  
change (Lin and Wu, 2011; Pu et al., 2021; Thackeray et al., 2016; Wegmann et al., 2017). For  
example, the reanalysis snow dataset (e.g., ERA40 and NCEP-NCAR) has revealed that  
anomalous snow cover in prior autumn facilitates a warm-north, cold-south winter over North  
65 America by influencing the teleconnection response in the Pacific-North American (PNA)  
region (Lin and Wu, 2011). Reanalysis datasets (e.g., MERRA, ERA-Interim, and GLDAS-2)  
have been integrated into the Canadian Sea Ice and Snow Evolution (CanSISE) dataset to  
analyze the impacts of global warming on snow changes on the TP (You et al., 2020a).

A comprehensive evaluation of multiple snow reanalysis datasets based on referenced  
70 observation data is of paramount importance before launching related scientific research.  
Previous researches have focused more on the accuracy of Snow Depth (SD) and Snow Water  
Equivalent (SWE) in reanalysis datasets across different regions (Bian et al., 2019; Li et al.,  
2022; Wang and Zeng, 2012; Zhang et al., 2021). However, only Orsolini et al. (2019) and Li  
et al. (2022) have assessed the SCF performance of reanalysis datasets over the High Mountain  
75 Asia based on SCF data from the Interactive Multisensor Snow and Ice Mapping System (IMS;  
Helfrich et al., 2007) and ground observations. Their studies considered the SCF accuracy of a  
limited number of reanalysis datasets and lacked multidimensional evaluation that considers  
aspects such as regional variations and annual trends, as well as an in-depth analysis of the  
impact of parameterization on SCF bias. In addition, the IMS dataset, which uses microwave  
80 remote sensing technology, is challenging for detecting shallow or wet snow that may lead to  
increased uncertainty in SCF detection (Yu et al., 2013). Therefore, prior evaluations of  
reanalysis SCF datasets are still insufficient.

The various reanalysis snow datasets have unique spatiotemporal characteristics (Mudryk  
et al., 2015). The differences in snow characteristics originate not only from the use of different  
85 Land Surface Models (LSMs), but also from the meteorological forcing data and  
parameterization methods. De Rosnay et al. (2014) indicated that the accuracy of snow  
simulations is constrained largely by uncertainties associated with some of the key

meteorological inputs, including precipitation and temperature (Cao et al., 2020; Zhang et al., 2015), under regional climate conditions and elevation factors (Brown and Mote, 2009; 90 Hernández-Henríquez et al., 2015). Therefore, uncertainties associated with precipitation and temperature data are likely to be the primary sources of bias within the reanalysis SCF datasets. Moreover, Jiang et al. (2020) emphasized that optimizing the parameterization methods used to convert SD or SWE to SCF would reduce the uncertainties associated with snow modeling, which would further reduce biases in land surface albedo simulations, particularly in high- 95 altitude regions. The reanalysis datasets use different SCF parameterization methods, with a 100% SCF corresponding to an SD that ranges from 2 to 26 cm (Orsolini et al., 2019). The selection of different SCF parameterizations for the reanalysis datasets may lead to varying degrees bias of SCF.

For this study, we conducted an in-depth evaluation of SCF simulations derived from eight 100 atmospheric and land assimilation reanalysis datasets over the period WYs 2001–2017, using SPIReS SCF dataset as a reference. The accuracy of SCF was assessed multidimensionally by examining the spatial characteristics, seasonal variations, and annual trends across the whole TP and its nine basins. Additionally, we aimed to assess the influence of meteorological forcing (snowfall and temperature) and the SCF parameterization on the SCF biases associated with the 105 various reanalysis datasets. On this basis, we attempted to develop an optimal combination of reanalysis SCF datasets.

## **2 Data and methods**

### **2.1 Data**

#### **2.1.1 Remote sensing data**

110 For this study, we utilized the SPIReS SCF dataset (Bair et al., 2021) as the reference SCF. It is derived from Landsat 8 Operational Land Imager (OLI) and MODIS data using a spectral unmixing methodology at a 4 km resolution for the period spanning WY 2000 to WY 2021 (e.g., WY 2000 refers to October 1, 1999, to September 30, 2000). The SCF calculation in SPIReS

relies on two endmembers (i.e., snow and snow-free) along with an ideal shade component,  
115 effectively simplifying the calculation process while maintaining high accuracy. SPIReS  
reduces the effects of cloud noise through interpolation and smoothing to provide more accurate  
SCF data (Bair et al., 2021; Dozier et al., 2008). In a comprehensive evaluation conducted by  
Stillinger et al. (2023) utilizing airborne lidar datasets for subcanopy snow mapping  
performance over mountain areas in the western United States, spectral unmixing-derived data  
120 (including SPIReS and MODIS Snow-Covered Area and Grain Size, abbreviated as  
MODSCAG) exhibited lower bias and Root Mean Square Error (RMSE) compared to data  
derived from band ratio methods and spectral mixture methods. Moreover, unlike MODSCAG,  
SPIReS incorporates the influence of light-absorbing particles on snow, leading to more  
accurate SCF data.

### 125 **2.1.2 Reanalysis datasets**

We examined eight widely used reanalysis datasets obtained from various meteorological  
organizations, with details listed in Table 1. Meteorological forcing fields are used to drive the  
LSMs, and parameterization methods are used to calculate the daily SCF data. The assimilation  
of snow data varied among the datasets.

130 The High Mountain Asia Snow Reanalysis (HMASR; Liu et al., 2021) is a snowpack-  
specific reanalysis dataset produced by NASA High Mountain Asia Team (HiMAT). HMASR  
uses the Simplified Simple Biosphere model, version 3 (SSiB3; Sun and Xue, 2001; Xue et al.,  
2003) as the LSM to generate the initial snowpack mass for WYs 2000–2017 based on  
meteorological inputs from MERRA2 and physiographic characteristics. The model-derived  
135 SCF predictions are then constrained by integrating spectral unmixing algorithm derived SCF  
data from the MODIS and Landsat satellites products (Painter et al., 2009) via data assimilation.  
The parameterization method used in HMASR (abbreviated as SSiB3\_SCF in Table 1) has not  
been publicly disclosed.

The Modern-Era Retrospective analysis for Research and Applications, version 2  
140 (MERRA2; Gelaro et al., 2017), developed by NASA's Global Modeling and Assimilation

Office (GMAO), provides land surface state estimates including SCF via the Catchment LSM (CLSM; Koster et al., 2000). The surface-forced precipitation is a combination of the National Oceanic and Atmospheric Administration (NOAA) Climate Prediction Center (CPC) unified gauge-based analysis of global daily precipitation (CPCU; Xie et al., 2007) product and the  
145 precipitation generated by the atmospheric general circulation model within the MERRA2 system. The generated precipitation is also adjusted using a precipitation correction algorithm (Reichle et al., 2017). MERRA2 does not include snow data assimilation. The parameterization scheme in MERRA2 considers 100% SCF to occur when the SWE reaches a threshold of 26 kg m<sup>-2</sup> (abbreviated as MM\_SCF in Table 1; Orsolini et al., 2019; Reichle et al., 2017).

150 The ECMWF Reanalysis version 5 (ERA5; Hersbach et al., 2020), produced and published by the European Centre for Medium-Range Weather Forecasts (ECMWF), uses the Tiled ECMWF Scheme for Surface Exchanges over Land (HTESSEL) model to simulate various land surface variables. The precipitation forcing in ERA5 is adjusted using Global Precipitation Climatology Project (GPCP; Adler et al., 2003) data. ERA5 assimilates in situ SD observations  
155 and binary SCF data from IMS only below 1500 m, so that snow assimilation does not apply to the TP region (Bian et al., 2019). Additionally, a refined dataset known as ERA5-Land (abbreviated as ERAL; Muñoz-Sabater et al., 2021) has been derived from ERA5 via the offline rerunning of the land portion of the model at a higher spatial resolution. ERA5L provides solely land surface parameters and is based on the same forcing and LSM as ERA5. Both datasets  
160 have a 10-cm SD threshold to identify full SCF (abbreviated as ME\_SCF in Table 1; ECMWF, 2018; Orsolini et al., 2019). ERA5 does not directly output the SCF variable. The SCF values for ERA5 used in this study was calculated using ME\_SCF method.

The Japanese 55-year Reanalysis (JRA55; Kobayashi et al., 2015), developed by the Japan Meteorological Agency (JMA), generates the land surface analysis field using an offline version  
165 of the Simple Biosphere (SIB) model (Sato et al., 1989; Sellers et al., 1986). The precipitation forcing is corrected using precipitable water retrieved from the Special Sensor Microwave/Imager (SSM/I) brightness temperature (Onogi et al., 2007). JRA55 incorporates daily SD data from the SSM/I and the Special Sensor Microwave Imager Sounder (SSMIS)

using a univariate two-dimensional optimal interpolation (OI) approach. In addition, it  
170 assimilates surface synoptic observations (SYNOP) reports and digitizes China's daily SD data  
from 1971 to 2006 (Onogi et al., 2007). The detection of full SCF in JRA55 is based on a 2-cm  
SD threshold (abbreviated as MJ\_SCF in Table 1; Orsolini et al., 2019). Similar to ERA5, the  
SCF in JRA55 was also calculated rather than provided directly by the product.

The Climate Forecast System Reanalysis (CFSR; Saha et al., 2010), developed by the  
175 National Center for Environmental Prediction (NCEP) under NOAA, is a weakly coupled  
global reanalysis system. The land surface analysis utilizes the Noah model (Meng et al., 2012).  
Two observed global precipitation analyses, namely the CPC Merged Analysis of Precipitation  
(CMAP; Xie and Arkin, 1997) and the CPCU, are used as alternative forcings for precipitation.  
In terms of snow analysis, CFSR assimilates IMS and the Global Snow Depth Model  
180 (SNODEP). On 1 January 2011, CFSR transitioned to a newer version of the NCEP data  
assimilation system called CFSv2 (Saha et al., 2014). Despite differences in horizontal  
resolution and minor changes to the physical parameterization, CFSv2 is considered a  
continuation of CFSR in most cases (Fujiwara et al., 2017). The SCF parameterization method  
in CFSR is related to the surface characteristics, using varying SD thresholds to identify the full  
185 SCF depending on the underlying surface type (abbreviated as Noah\_SCF in Table 1; Ek et al.,  
2003).

The Global Land Data Assimilation System version 2.1 (GLDAS-2.1; Rodell et al., 2004)  
is a global land data assimilation product developed jointly by NASA and NOAA. It uses the  
global meteorological forcing dataset from Princeton University (Sheffield et al., 2006) and the  
190 GPCP V1.3 Daily Analysis precipitation fields (Adler et al., 2003; Huffman et al., 2001) to  
drive three distinct LSMs: the CLSM model, the Noah model, and the Variable Infiltration  
Capacity (VIC) model. As a result, four datasets are generated (Table S1). Notably, the full  
series datasets within GLDAS-2.1 do not assimilate snow observations. Furthermore, owing to  
the unavailability of SCF variables in these datasets, this study derived different SCF values  
195 using three parameterization methods (MM\_SCF, ME\_SCF and MJ\_SCF). Finally, the  $0.25^\circ \times$



0.25° GLDAS–Noah product using the MM\_SCF approach was selected as a representative of GLDAS due to its better SCF simulation (Fig. S1).

China’s First Generation Global Atmospheric and Land Reanalysis (CRA-40; Liu et al., 2023) is produced by the China Meteorological Administration (CMA). The matched land surface reanalysis datasets (CRA-40/Land, abbreviated as CRAL) are simultaneously generated offline based on an updated version of the Noah model and atmospheric driving factors from CRA-40. In CRAL, precipitation meteorological forcing is derived from a similar combination of data sources as CFSR (Liang et al., 2020). CRAL does not assimilate other observational data in the LSM. Instead, data from over 2,400 CMA surface weather observatories indirectly influence the land surface product through conventional meteorological forcing derived from atmospheric reanalysis (Liang et al., 2020). The SCF parameterization method in CRAL is the same as that in CFSR.

**Table 1: Characteristics of the reanalysis datasets used in this study.**

Reanalysis dataset	Agency	Temporal coverage	Resolution	Land Model	Snow data assimilation	Variables used in analysis <sup>b</sup>	SCF parameterization method used in this study	Reference dataset
HMASR	NASA HiMAT	WY 1999 to WY 2017	1/225°×1/225°	SSiB3	MODIS and Landsat	SCF, SWE, SD	SSiB3_SCF	Liu et al., (2021)
MERRA2	NASA GMAO	1980 to present	0.625°×0.5°	Catchment	-	SCF, SWE, SD, T2, Snowfall	SCF= min (1, SWE/26) <sup>a</sup>	Gelaro et al., (2017)
ERA5	ECMWF	1979 to present	0.25°×0.25°	H-TESEL	-	SWE, SD, T2, Snowfall, RH	SCF= min (1, (SD)/10) <sup>a</sup>	Hersbach et al., (2020)
ERA5L	ECMWF	1981 to present	0.1°×0.1°	H-TESEL	-	SCF, SWE, SD, T2, Snowfall	SCF= min (1, (SD)/10) <sup>a</sup>	Muñoz-Sabater et al., (2021)
CRAL	CMA	1979 to present	0.5°×0.5°	Noah	-	SCF, SWE, SD, T2, Snowfall	Noah_SCF	Liu et al., (2023)
JRA55	JMA	1958 to present	0.563°×0.563°	SiB	Station, SSM/I, SSMIS	SWE, SD, T2, Snowfall	SCF= min (1, (SD)/2) <sup>a</sup>	Kobayashi et al., (2015)
CFSR	NOAA NCEP	1979 to present	0.5°×0.5°	Noah	SNODEP, IMS	SCF, SWE, SD, T2, Snowfall	Noah_SCF	Saha et al., (2010); Saha et al., (2014)
GLDAS	NASA and NOAA	2000 to present	0.25°×0.25°	Noah	-	SWE, SD, T2, Snowfall	MM_SCF	Rodell et al., (2004)

<sup>a</sup> The unit for SWE is kg m<sup>-2</sup>, and for SD is cm. <sup>b</sup> ERA5, JRA55, and GLDAS do not provide output for the SCF variable directly. In this study, the SCF values for ERA5 and JRA55 were derived using their respective parameterization methods, as shown in the Table 1. The SCF values for GLDAS were derived using MERRA2 parameterization methods. T2 is 2-m air temperature.

### 2.1.3 Meteorological dataset

215 To investigate the effects of snowfall and temperature biases on SCF bias, we used precipitation  
and 2-m air temperature data from the high-resolution near-surface Meteorological Forcing  
Dataset for the Third Pole region (TPMFD; Yang et al., 2023) as the reference data.  
Precipitation and 2-m air temperature in TPMFD were derived by combining a short-term high-  
220 resolution Weather Research and Forecasting (WRF) simulation (Zhou et al., 2021), long-term  
ERA5 data, and in situ observations, all at a resolution of  $1/30^\circ$  for the period spanning 1979  
to 2020. Validation conducted by Jiang et al. (2023) demonstrated that the precipitation data  
from TPMFD are unbiased overall and considerably better than other widely used datasets. To  
obtain snowfall data for this study, we applied a dynamic threshold parameterization scheme,  
which considers surface air conditions such as wet bulb temperature, altitude, and relative  
225 humidity, to convert TPMFD total precipitation to snowfall. This approach has been proven  
effective in capturing snowfall variations on the TP through comparisons with station  
observations (Ding et al., 2014) and has been used in many studies (Deng et al., 2017; Luo et  
al., 2020; Yang et al., 2021; Zhu et al., 2021). For detailed calculation methods and further  
information, readers are referred to the work of Ding et al. (2014). We note that TPMFD lacks  
230 the relative humidity variable necessary for snowfall conversion, while all variables in TPMFD  
are assimilated from ERA5 data. Therefore, we utilized ERA5 surface relative humidity as a  
substitute.

### 2.2 Study region

The boundary of the TP used in this study is identified as an isoline of 2,500 m according to the  
235 Global Multi-resolution Terrain Elevation Data 2010 (Danielson and Gesch, 2011), spanning  
from  $26^\circ\text{N}$  to  $41^\circ\text{N}$  and from  $67^\circ\text{E}$  to  $105^\circ\text{E}$  (Fig. 1b). The prevailing westerlies and monsoons  
are the primary moisture sources in this region, exerting significant influence on the spatial and  
temporal distribution of snowfall and glacier mass balance (Liu et al., 2021; Yao et al., 2012).  
Specifically, the westerlies dominate winter precipitation, while the Indian and East Asian  
240 monsoons dominate summer precipitation in the southeast (Yao et al., 2012), resulting in

diverse snow regimes. We identified nine major river basins within the TP using Hydrological Data and Maps Based on Shuttle Elevation Derivatives at Multiple Scales (HydroSHEDS; Lehner et al., 2008), namely the Amu, Indus, Tarim, Inner Tibetan Plateau (ITP), Brahmaputra, Salween, Mekong, Yangtze, and Yellow basins. Due to the differing impacts of winter and summer atmospheric forcing, the performance of SCF simulations from reanalysis datasets varies across these basins.

## 2.3 Methods

### 2.3.1 Evaluation of SCF accuracy for reanalysis datasets

In this study, we used time series spanning from WYs 2001–2017, covering periods for which all data were available. Before evaluation, all data were regridded to a  $0.5^\circ \times 0.5^\circ$  grid via bilinear interpolation for MERRA2, JRA55, and CRAL, and the grid averaging approach for HMASR, ERA5, ERA5L, GLDAS, SPIReS, and TPMFD.

For each  $0.5^\circ \times 0.5^\circ$  grid cell within the TP, we calculated the climatological SCF over the full period and seasonally for SPIReS and eight reanalysis datasets (e.g., Fig. 1a and Fig. S3). Absolute bias and correlation (Pearson’s correlation coefficient) were calculated from these values at both the basin and the TP scales. Spatial distribution and basin-averaged values of the climatological SCF, as well as bias maps of the reanalysis datasets compared to SPIReS, are presented. Additionally, Taylor diagrams are used to provide additional information regarding the RMSE and standard deviation ratio (STDR). The climatological SCF values for each grid cell within basin and region were used as input to calculate the Taylor Diagram’s component metrics (correlation, RMSE, and STDR). The component metrics were summarized by the Taylor Skill Score (SS) as follows:

$$SS = \frac{4(1+R)^4}{(STDR + 1/STDR)^2(1+R_0)^4} \quad (1)$$

where  $R_0$  is the maximum correlation attainable.

The Mann-Kendall (MK; Kendall, 1975; Mann, 1945) test was used to assess the significance of annual trends. Since the sign (+ or –) may impact the robustness of the trend analysis results, we employed the Consistency Index (CI; Zhang et al., 2021) to compare the

agreement in SCF annual trend signs between the reanalysis datasets and SPIReS. The CI is defined as follows:

$$270 \quad CI = \frac{N_{inc} + N_{dec} + N_{no}}{N_{tot}} \quad (2)$$

where  $N_{inc}$  is the number of grid points with a significant increasing trend in both the reanalysis dataset and SPIReS ( $P < 0.05$ ),  $N_{dec}$  is the number of grid points with a significant decreasing trend in both datasets,  $N_{no}$  is the number of grid points with a non-significant trend in both datasets, and  $N_{tot}$  is the total number of grid points. The higher the CI value, the better  
275 the performance of the trend simulation.

### 2.3.2 Analysis of SCF bias sources for meteorological forcings

Variations in snowfall and temperature are the dominant influences on snow evolution and can explain half to two-thirds of the interannual variability in snow cover (Xu et al., 2017). Hence, biases in snowfall and temperature within reanalysis datasets are likely the main sources of bias  
280 in SCF. Here, the analysis of bias sources was primarily based on correlation analysis between the bias of SCF and those of snowfall and temperature. The absolute biases of snowfall and temperature were computed by comparing the reanalysis datasets with TPMFD. Additionally, we calculated the correlation between the annual time series of snowfall and temperature biases at each TP grid cell and SCF bias to obtain the spatial distribution of correlations as shown in  
285 Fig. 6.

### 2.3.3 Analysis of SCF bias sources for parameterization method

Evaluations have shown that in the TP, with relatively thin and short-lived snow (Huang et al., 2023), optimizing the SCF parameterization can significantly reduce the annual SCF bias in snow models (Jiang et al., 2020). Orsolini et al. (2019) noted that SCF parameterization differs  
290 significantly among reanalyses, affecting SCF bias. For the eight reanalysis datasets considered here, five parameterizations were used to convert SWE or SD into SCF; i.e., MM\_SCF, ME\_SCF, MJ\_SCF, SSiB3\_SCF, and Noah\_SCF (see Section 2.1.2 and Table 1). In order to evaluate the impact of the parameterization on SCF simulations, we incorporated three publicly

available and easily offline-usable parameterization methods (MM\_SCF, ME\_SCF, and  
295 MJ\_SCF) separately into each reanalysis dataset. For HMASR, CRAL, and CFSR, which do  
not include their parameterization among these three methods, we derived three additional SCF  
datasets. MERRA2, ERA5, ERA5L, JRA55, and GLDAS derive another two SCF datasets.

### **2.3.4 Generation of combined optimal datasets**

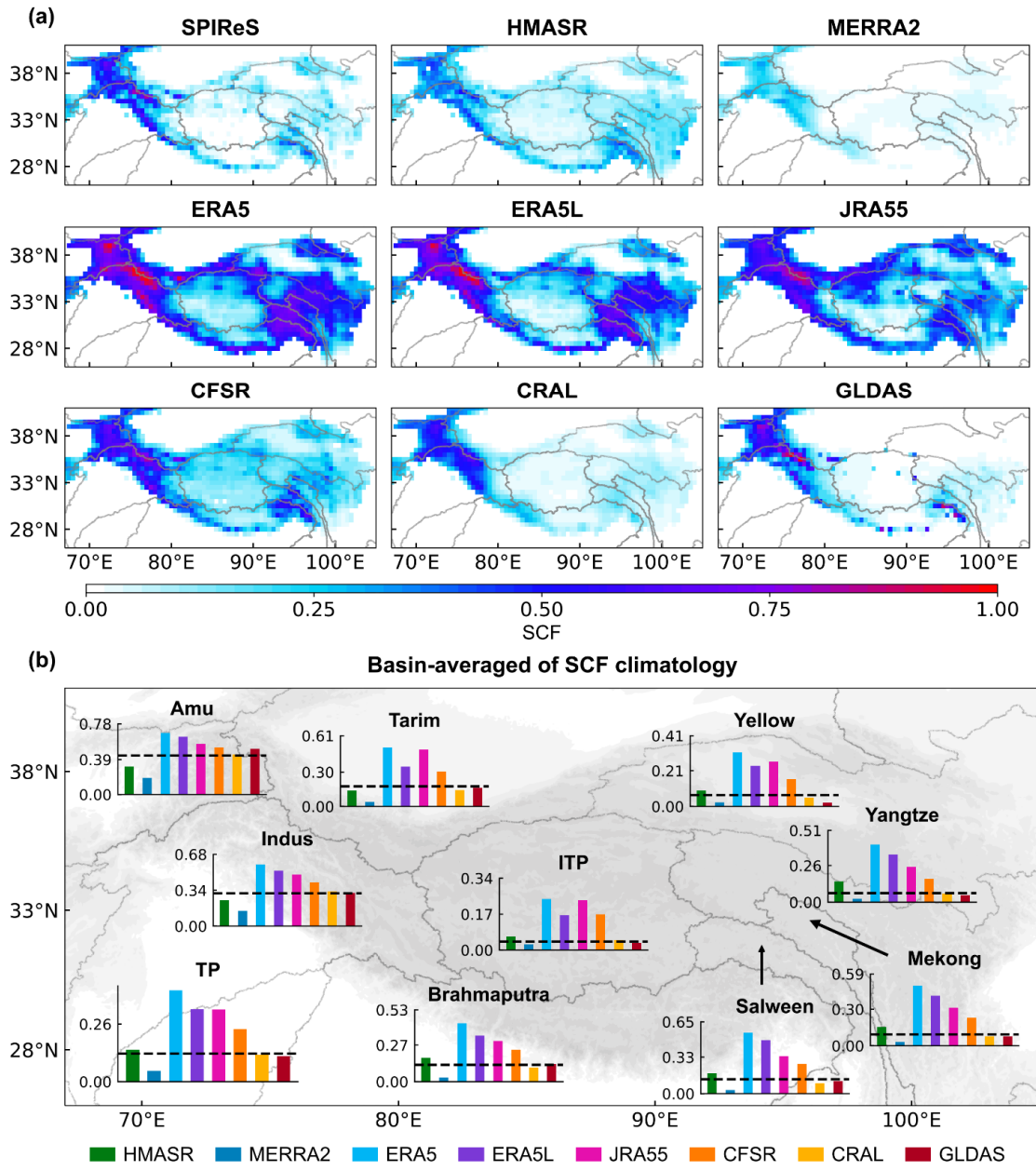
Mortimer et al. (2020) demonstrated that product accuracy can be enhanced by averaging  
300 multiple reanalysis datasets, as this allows unrelated errors and deficiencies between them to  
offset each other. To investigate whether averaging of multiple datasets can improve SCF  
accuracy over the complex terrain of the TP, we considered all possible combinations of the  
eight reanalysis datasets, totaling 247. The output of each combined dataset was computed as  
the equally weighted average of all reanalysis datasets in the combination (Mudryk et al., 2015).  
305 Subsequently, we characterized the SCF accuracy of combined datasets in spatial distribution  
and annual trends by computing the SS and CI values.

## **3. Results**

### **3.1 Evaluation of spatial and temporal accuracy in SCF**

#### **3.1.1 Spatial variability of SCF climatology and seasonality**

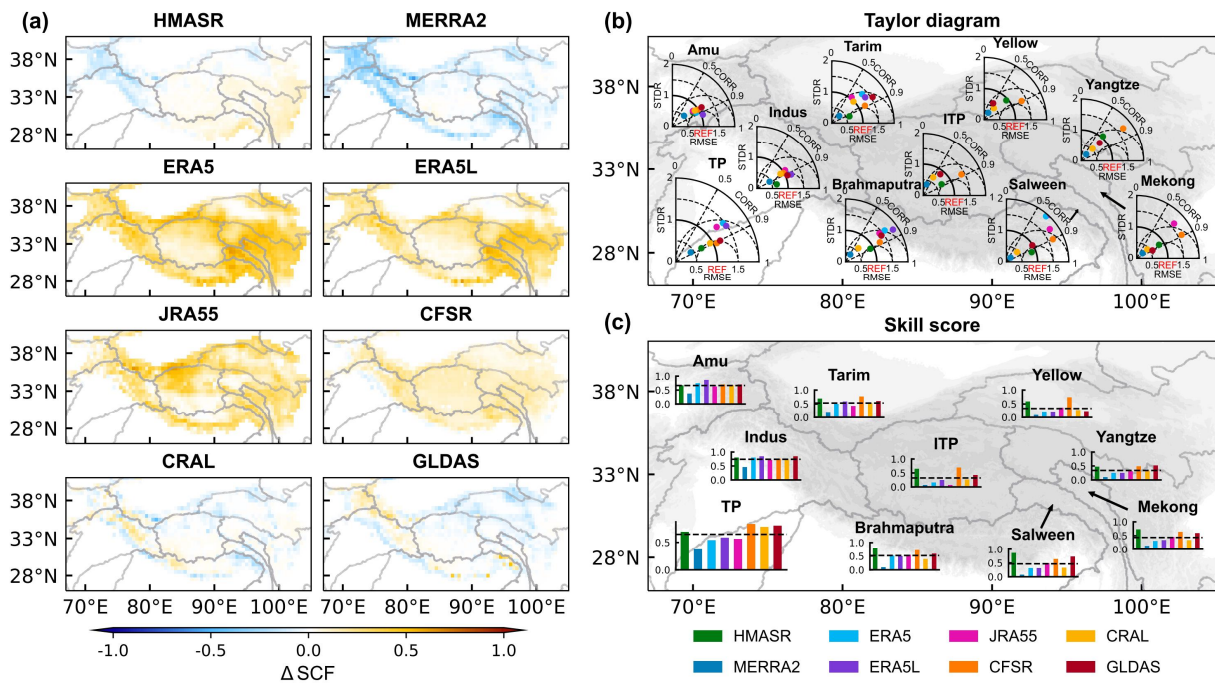
310 The TP-averaged SCF for HMASR, GLDAS, and CRAL is 0.14, 0.12, and 0.12, respectively,  
which align closely with the SPIReS value of 0.13 (Fig. 1b). HMASR (GLDAS and CRAL)  
slightly underestimates (overestimate) in westerlies-dominated basins such as the Amu and  
Indus, and overestimates (underestimate) in monsoon-dominated basins such as the Yellow,  
Yangtze, Mekong, Salween, and Brahmaputra (Fig. 2a). These regional biases average out when  
315 considering the entire TP, which is reflected in the strong permanence of these datasets over the  
TP. Conversely, ERA5, ERA5L, and JRA55 have large positive SCF biases across all basins,  
whereas MERRA2 has a negative bias in all basins. Over the TP as a whole, ERA5 (MERRA2)  
has the largest positive (negative) bias.



320 **Figure 1: (a) Spatial distribution of Snow Cover Fraction (SCF) climatological average for Water Years (WYs) 2001–2017 from SPIReS and eight reanalysis datasets over the Tibetan Plateau region. (b) Basin-averaged of SCF climatology from SPIReS (black horizontal line) and the eight reanalysis datasets overlain on a map of the TP. ITP = Inner Tibetan Plateau.**

325 All datasets have similar spatial patterns of SCF, with higher values in the western TP and lower values in the interior (Fig. 1a). However, compared to SPIReS, the magnitude and sign of their biases vary spatially (Fig. 2a). This variation is demonstrated by their differing correlation, STDR, and RMSE values (Fig. 2b; see Fig. S2 for a clearer version) and hence their SS values (Fig. 2c) between the reanalysis datasets and SPIReS. CFSR has the highest SS value

330 of 0.83, reflecting its strong correlation in westerlies-dominated basins and variability close to  
 that of SPIReS in monsoon-dominated basins (STDR close to 1, e.g., 0.98 for the Indus basin).  
 The SS values for GLDAS, CRAL, and HMASR are all above 0.7, benefiting from their high  
 correlations similar to CFSR. Consequently, these four datasets have superior SCF spatial  
 performance across the TP. In contrast, although ERA5, ERA5L, and JRA55 can adequately  
 335 capture the STDR in monsoon-dominated basins, their large positive biases lead to high RMSE,  
 resulting in moderate SS values across the TP. MERRA2 has the worst spatial performance,  
 with the lowest SS value in all basins and across the TP. This contradicts Orsolini et al. (2019),  
 who found MERRA2 to perform well in capturing the SCF and SD characteristics. This  
 discrepancy arises because their results depended mainly on the high correlation between  
 340 MERRA2 and the reference dataset, ignoring severe underestimations in SCF values. These  
 underestimations result in very small self-standard deviations in the STDR calculation, leading  
 to the lowest SS value.

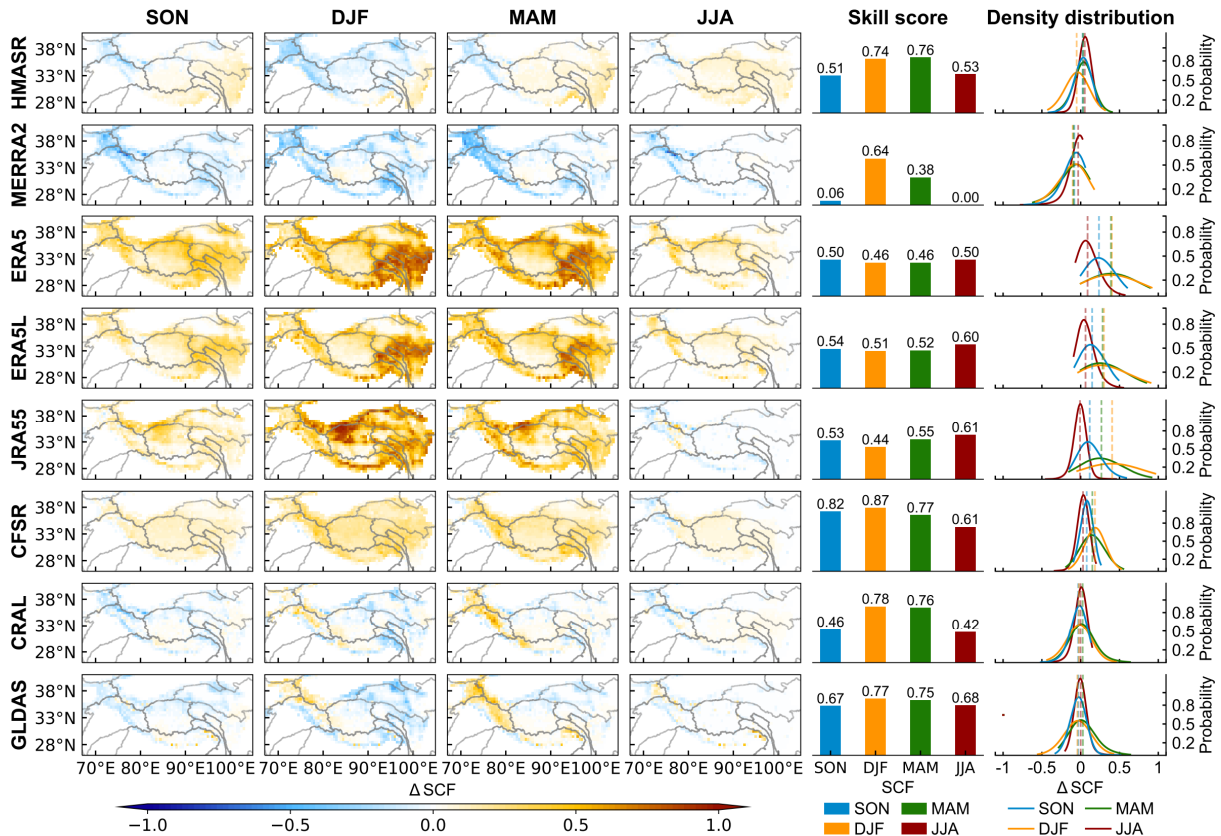


345 **Figure 2: (a) Spatial distribution of the SCF climatological bias from the reanalysis datasets based on SPIReS over the TP. (b) Taylor diagrams showing the correlation coefficients (R), Root Mean Square Error (RMSE), and Standard Deviation Ratio (STDR) of SCF between reanalysis datasets and SPIReS for each basin, overlain on a map of the TP. (c) Taylor Skill Scores (SS) for each basin overlain on a map of the TP. The black line is the average of the SS values for all reanalysis datasets in basin.**

350 Basins affected primarily by the winter westerlies (e.g., the Amu and Indus basins) have better spatial performance, with the SS values for all reanalysis datasets within these basins exceeding 0.66 (Fig. 2c). In basins influenced by the summer monsoon (e.g., the Yellow, Yangtze, Mekong, Salween, and Brahmaputra basins), SCF spatial consistency with SPIReS varies. The basin-averaged of SCF climatology is highly biased in the Yellow and Yangtze  
355 basins for reanalysis datasets (Fig. 1b). Specifically, the basin-averaged SCF values of ERA5, ERA5L, and JRA55 (MERRA2) are more than 2× larger (lower) than SPIReS. These biases result in varied RMSE and STDR among these reanalysis datasets (Fig. 2b) and lower SS values (Fig. 2c). However, this phenomenon is less pronounced in the Salween and Brahmaputra basins. The Tarim and ITP basins are considered inland basins. In particular, the ITP basin  
360 shows the poorest SCF spatial performance among basins, with the reanalysis average SS values only 0.33.

Figure 3 shows the SCF bias, its probability density distribution, and the SS values for four seasons. In general, the different seasons have similar spatial patterns of SCF bias for each reanalysis dataset (Fig. 3, first to fourth columns on left). However, there are seasonal variations  
365 in the bias magnitudes, with larger biases during the accumulation period (winter and spring) and smaller biases during the ablation period (summer and autumn). The largest bias in winter can be several times larger than the lowest bias in summer. This is because higher seasonal averages of SCF (Fig. S3) may induce larger seasonal bias. Additionally, correlation and STDR (Table S2), and hence SS (Fig. 3, fifth column on left), are better during the accumulation period,  
370 indicating that winter and spring have better spatial performance for SCF. MERRA2 and CRAL have the largest seasonal variability in SCF performance (Fig. 3, sixth column on left).





375 **Figure 3:** The first four columns show the spatial distribution of seasonal SCF climatological bias from the reanalysis datasets based on SPIReS over the TP during (left to right): autumn (September–November: SON), winter (December–February: DJF), spring (March–May: MAM), and summer (June–August: JJA). The SS values of seasonal SCF climatology are shown in the fifth column. The probability density distribution of seasonal SCF climatological bias is shown in the sixth column. The dashed lines in the sixth column represent the TP-average SCF bias for each season.

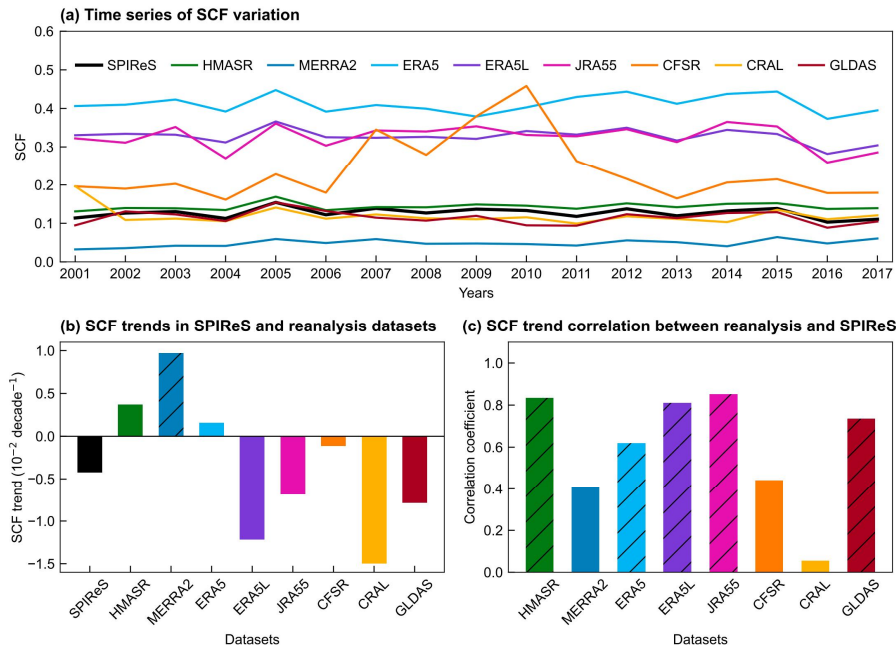
380

### 3.1.3 Annual variability and trends in SCF

The 17 WY time series of reanalysis datasets has spatially consistent overestimates for ERA5L, ERA5, and JRA55 and an underestimate for MERRA2 (Fig. 4a). Notably, the fluctuations in CFSR around 2010 align with variations in its temperature and snowfall (Fig. S4), likely due to inherent discontinuities in the dataset that cause changes in boundary conditions and subsequently in model output variables (Fujiwara et al., 2017). Additionally, the annual variation of TP-averaged SCF has no significant annual trend in SPIReS (Fig. 4b). ERA5L, JRA55, and GLDAS have annual trends consistent with SPIReS, showing a slight decline and significant correlation, with correlation coefficients above 0.7 (Fig. 4c). Although HMASR and

385

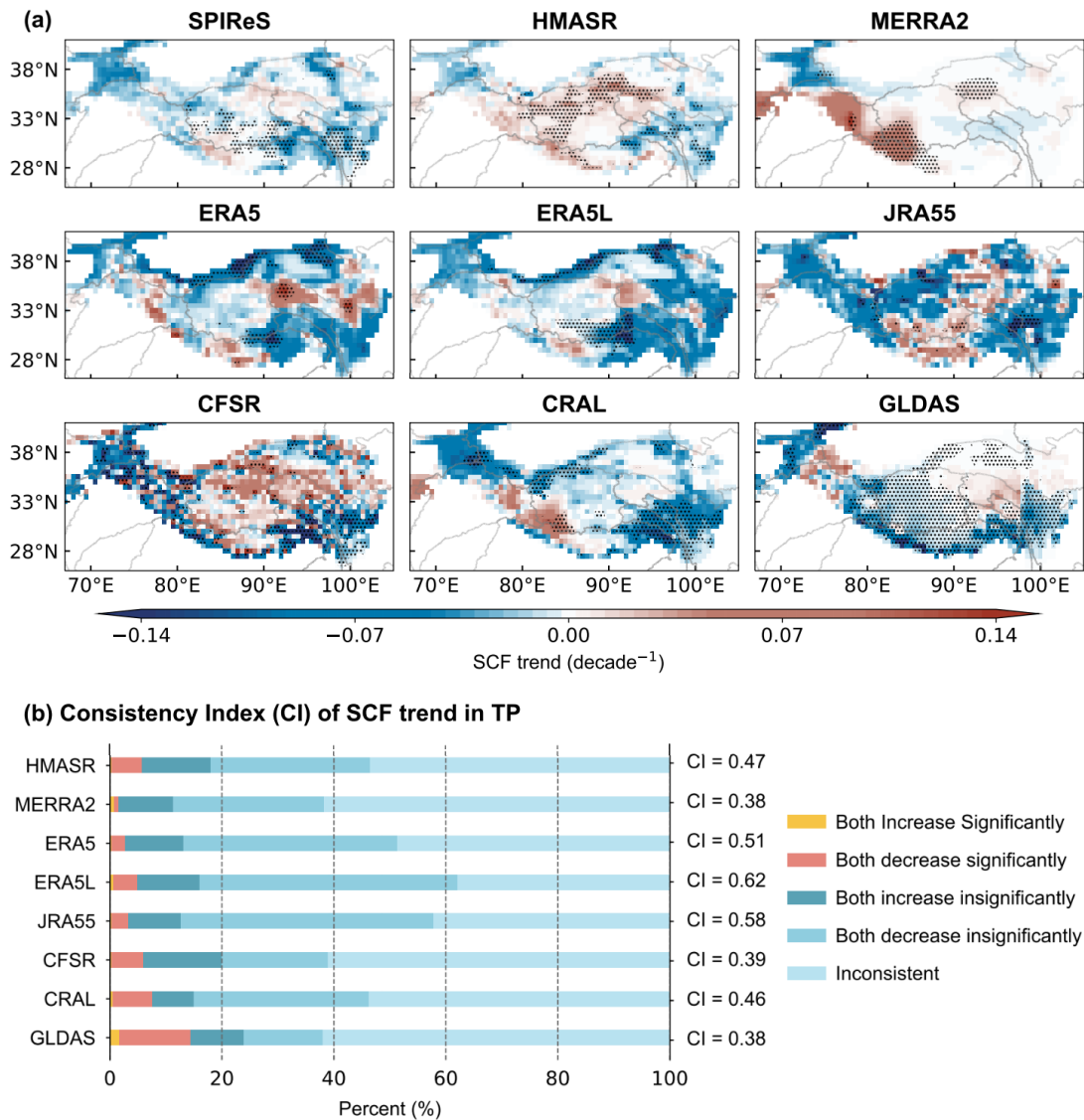
390 ERA5 have a slight increasing trend, they remain significantly correlated with SPIReS. Conversely, the correlation of MERRA2, CFSR, and GLDAS with SPIReS did not pass the statistical significance test.



395 **Figure 4: (a) Time series of the annual SCF from SPIReS and eight reanalysis datasets over the TP. (b) The annual trends of SCF from SPIReS and eight reanalysis datasets over the TP. (c) The correlation of SCF annual trends in reanalysis datasets with SPIReS over the TP. Slashes in (b) and (c) indicate that the annual trends and correlation exceeds the 95% confidence level.**

We further evaluated the spatial consistency of annual trends in reanalysis datasets with SPIReS (Fig. 5). SPIReS have generally decreased SCF over the westerlies-dominated and the eastern and southeastern monsoon-dominated basins, but increased SCF in the northeastern ITP, the central Brahmaputra, and the northern Yangtze basins. However, these changes are statistically significant in only about 17% of the TP (Fig. 5a). ERA5L, JRA55, and ERA5 have greater variability in SCF annual trends, with significant decreases in the Tarim basin. Nevertheless, they still have relatively high CI values of 0.62, 0.58, and 0.51, respectively (Fig. 5b). This indicates that ERA5L, JRA55, and ERA5 can capture more than half of the SCF annual trend changes over the TP, having the most similar spatial pattern of annual trends compared to SPIReS. In contrast, CFSR has highly uneven SCF annual trends with intermixed increases and decreases across grid cells, resulting in poorer trend performance with a CI value of only 0.39. MERRA2 exhibits significant increasing trends in the Indus basin but fails to

capture the correct decreasing trend in the monsoon-dominated basins. Consequently, it has the lowest CI value of 0.38, with CI values below 0.4 in most basins (Fig. S6). GLDAS has a significant decrease in SCF over more than 60% of the TP, notably differing from SPIReS. Although the widespread significant trends allow GLDAS to capture the most correct significant increase and decrease trends, reaching 16.42% (as indicated by the red and yellow bars in Fig. 5b), it also introduces a major drawback by misjudging too many insignificant SCF fluctuations. Therefore, GLDAS has the lowest CI value, similar to MERRA2. Combination of SCF time series and spatial consistency of SCF annual trend, ERA5L, JRA55, and ERA5 have better temporal performance, while CFSR, MERRA2, and GLDAS perform worse.



420

**Figure 5: (a) Spatial distribution of the SCF annual trend from SPIReS and eight reanalysis datasets over the TP for the period WY 2001 to WY 2017. (b) The Consistency Index (CI) of SCF trends in reanalysis datasets with SPIReS over the TP.**

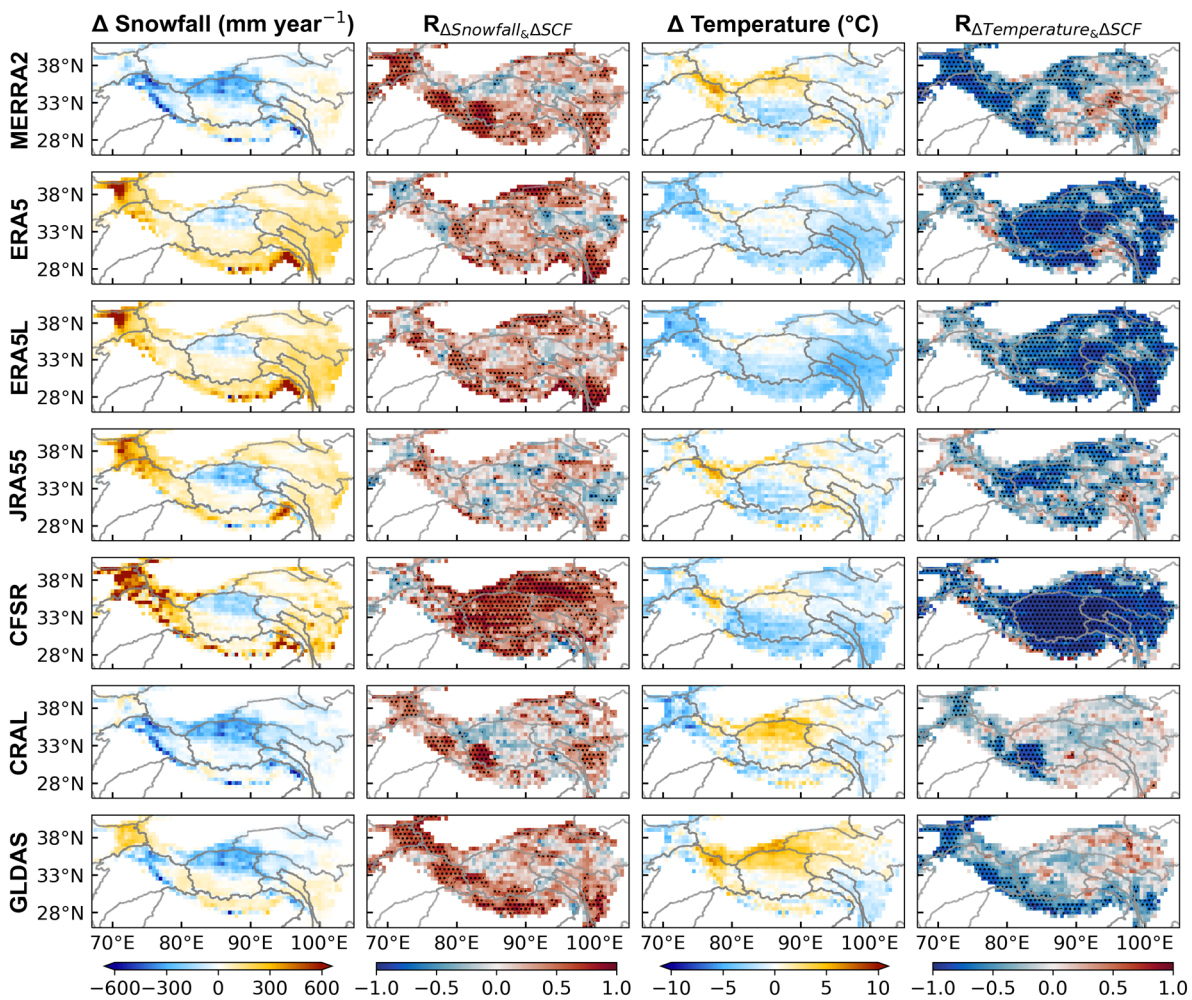
## 3.2 Bias attribution of SCF

### 425 3.2.1 Meteorological forcing effects on SCF bias

The evolution of SCF can be determined from the balance between snow mass gain via snowfall and snow depletion via snowmelt, sublimation, and wind drifting (Liu et al., 2022). Both snowfall and snowmelt are strongly dependent on temperature (Serquet et al., 2011; Vorkauf et al., 2021). Hence, the accuracy of snowfall and temperature forcings impacts the accuracy of  
430 snow-related variables (Zhang et al., 2015). We investigated the impact of meteorological factors on SCF bias by examining the performance with respect to snowfall and temperature in each reanalysis dataset.

In the climatological spatial distribution, ERA5, ERA5L, JRA55, and CFSR overestimate snowfall in both the westerlies-dominated and monsoon-dominated basins, particularly in the  
435 Indus and Brahmaputra basins (Fig. 6, first column on left). Conversely, these reanalysis datasets consistently underestimate temperatures in these regions (Fig. 6, third column on left). Overestimated snowfall contributes to heightened snow accumulation, while underestimated temperatures can impede the snowmelt process, leading to an overestimation of snow cover (Liu et al., 2022). The combination of overestimated snowfall and underestimated temperatures  
440 contributes to the positive SCF bias observed in ERA5, ERA5L, JRA55, and CFSR, evidenced by the significant correlations between snowfall and temperature biases and SCF bias (Fig. 6, second and fourth columns on the left). Additionally, the positive SCF and snowfall biases, as well as negative temperature bias for these reanalysis datasets persist across four seasons, reflecting that the uncertainties in snowfall and temperature data affect the SCF bias year-round  
445 (Fig. 7). Compared to snowfall, temperature bias have higher correlations with SCF bias and pass significance tests over broader areas (Fig. 6, second and fourth columns on the left). This indicates that physical processes influenced by temperature bias may have a more pronounced and widespread responsibility with respect to SCF bias. The temperature biases in ERA5, ERA5L, JRA55, and CFSR also appear to have a greater impact on the seasonal evolution of  
450 SCF biases, as evidenced by the higher correlation values (Fig. 7). For MERRA2, CRAL and

GLDAS, the SCF climatology has large biases in the westerlies-dominated basins, as well as in the Tarim and Brahmaputra basins (Fig. 2a), where a significant correlation exists between snowfall and temperature biases and SCF bias (Fig. 6, second and fourth columns on the left). This suggests that in these regions, both snowfall and temperature play equally important roles in influencing the SCF biases in MERRA2, CRAL and GLDAS. When considering the TP as a whole, the SCF biases across four seasons for these three datasets align with their well-simulated snowfall (Fig. 7). Therefore, snowfall is likely the primary driver of the seasonal SCF bias.



460 **Figure 6: The columns show (from left to right): spatial distribution of the snowfall climatological bias for the reanalysis datasets based on TPMFD over the TP; spatial distribution of the R value between snowfall bias and SCF bias; spatial distribution of the temperature climatological bias for the reanalysis datasets based on TPMFD over the TP; and spatial distribution of R values between temperature bias and SCF bias. Black dots**  
 465 **in the second and fourth columns indicate that the correlation exceeds the 95% confidence level. HMASR and MERRA2 share the same meteorological forcing data.**



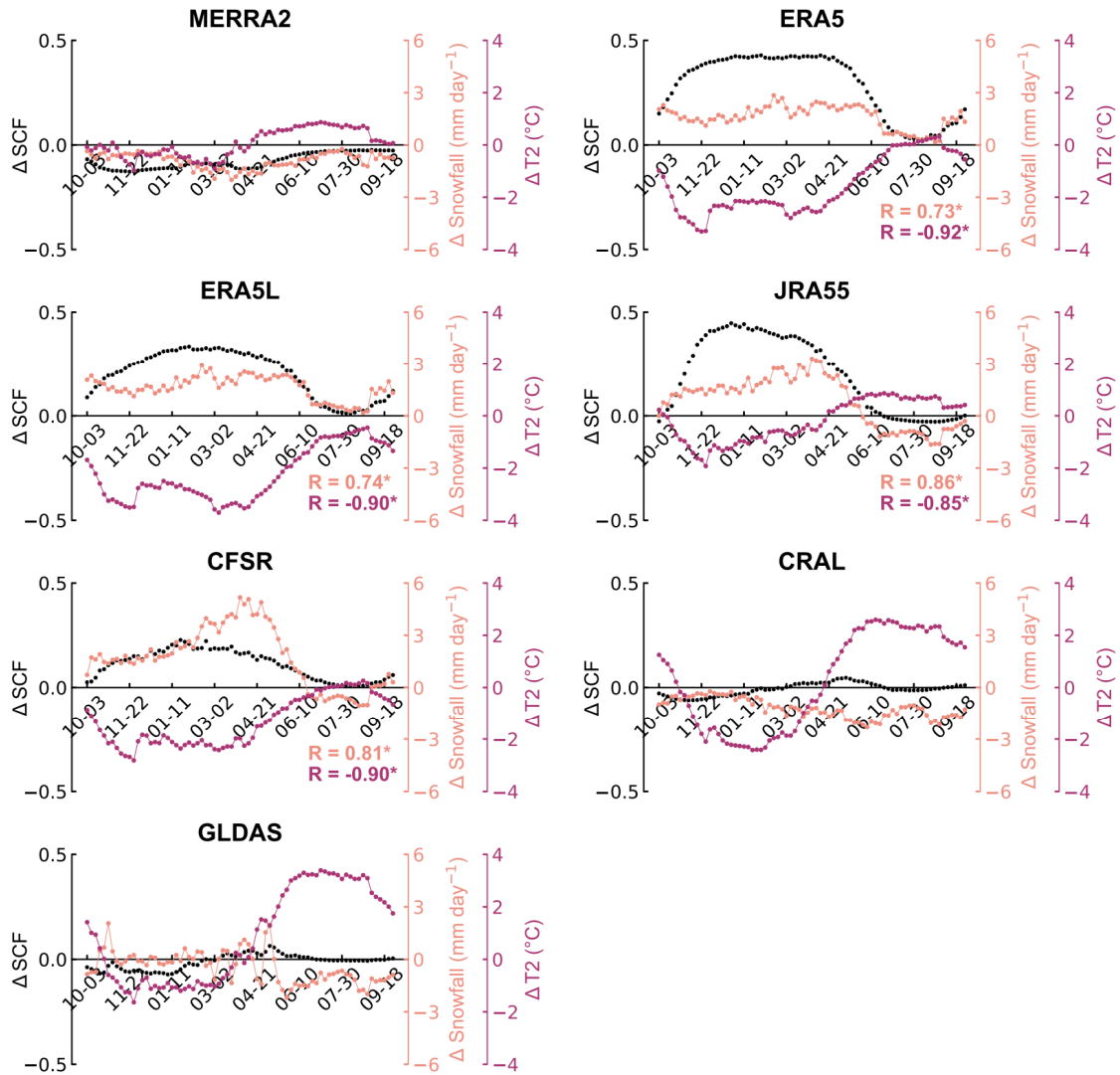


**Figure 7: Temporal variations of SCF (black), snowfall (light pink), and temperature (purple) bias averaged at five-day intervals from all reanalysis datasets. R in light pink (purple) represents the correlation coefficient between snowfall (temperature) bias and SCF bias. The stars indicate the correlation exceeds the 95% confidence level. HMASR and MERRA2 share the same meteorological forcing data.**

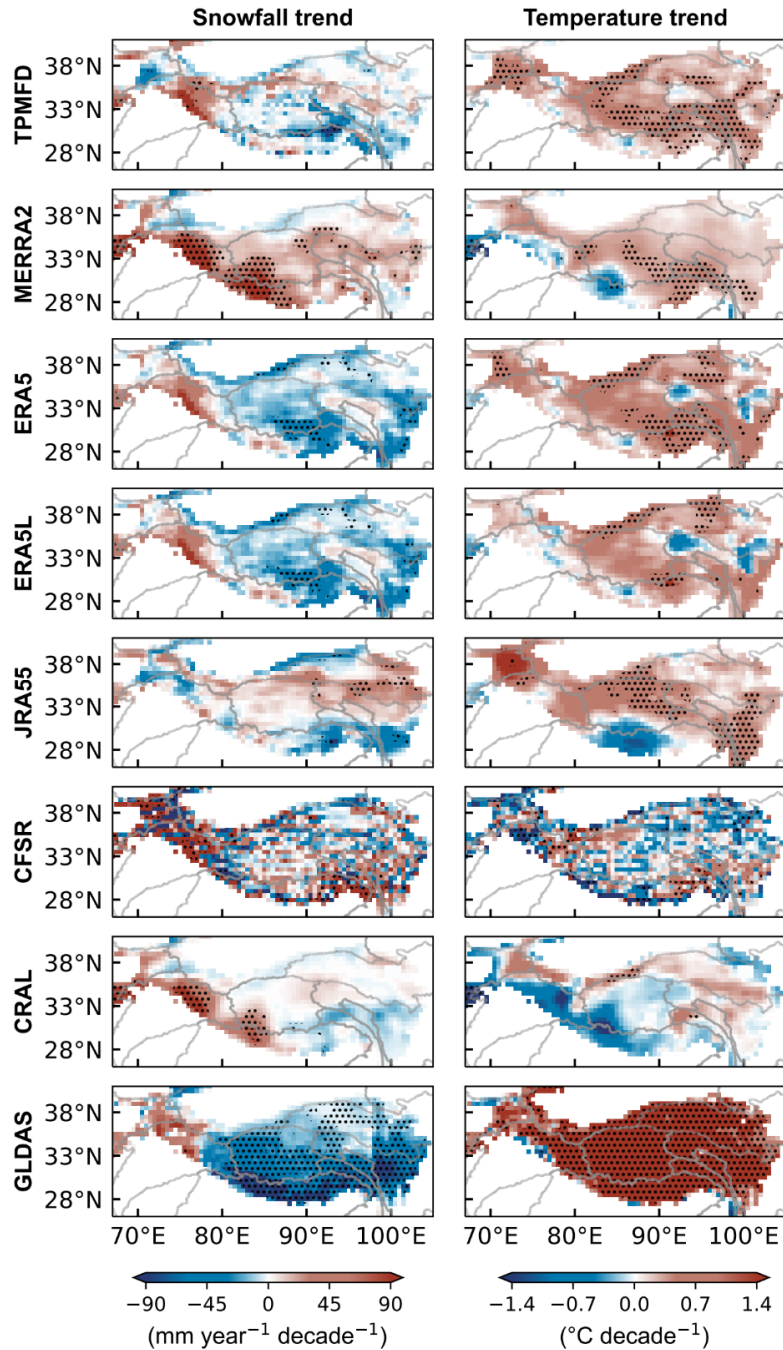
470

475

480

The snowfall and temperature annual trends in most datasets are significantly correlated with their own SCF annual trends (Table S3), indicating that the ability of datasets to capture meteorological factors annual trends influences the simulation of SCF annual trends. ERA5L, JRA55, and ERA5 have correct decreasing snowfall trends and increasing temperature trends in the southeastern monsoon-dominated basins (Fig. 8). Their CI values for meteorological factors trends all exceed 0.5, showing better spatial consistency with TPMFD (Table 2), resulting in better SCF trend simulations. In contrast, MERRA2 has an incorrect significant increase in snowfall over a broad region, except for the Tarim basin (Fig. 8), resulting in a

snowfall CI value of only 0.34 (Table 2) and poorer SCF trend simulations. The highly uneven spatial distribution of annual snowfall and temperature trends in CFSR, as well as the widespread significant trends in GLDAS (with temperature trends significantly increasing in over 90% of the TP), mirror their respective SCF annual trend patterns (Fig. 8). Consequently, 485 CFSR and GLDAS have the lowest CI values for SCF trends (Fig. 5b).



490 **Figure 8: Spatial distribution of the snowfall annual trend from the reanalysis datasets over the TP for the period WY 2001 to WY 2017 (left), and the temperature annual trend (right). Black dots indicate that the trend exceeds the 95% confidence level. HMASR and MERRA2 share the same meteorological forcing data.**

**Table 2: CI value for snowfall and temperature from eight reanalysis datasets calculated by comparing with TPMFD annual trends from WY 2001 to WY 2017.**

	CI values for snowfall	CI values for temperature
MERRA2	0.34	0.58
ERA5	0.54	0.73
ERA5L	0.55	0.59
JRA55	0.54	0.51
CFSR	0.37	0.29
CRAL	0.53	0.30
GLDAS	0.21	0.35

### 3.2.2 Parameterization approach effects on SCF bias

Different SCF parameterizations influence the instability inherent in the snow models (Dutra et al., 2011; Jiang et al., 2020). We considered the impact of different parameterizations on the spatial distribution and annual trend simulation of SCF for each reanalysis dataset (Fig. 9). The parameterization process primarily affects the SCF values, while its impact on the phase of fluctuations in SCF time series is limited, as evidenced by the small variations in CI values among the reanalysis datasets (Fig. 9b). Therefore, the focus is on the spatial performance of the parameterization-improved SCF simulation, reflecting by the spatial distribution of SCF bias (Fig. S7) and SS values (Fig. 9a).

The MM\_SCF method improves the SCF spatial simulation in ERA5, ERA5L, JRA55, HMASR, and CFSR, reducing biases and increasing SS values, demonstrating its broad applicability. Meanwhile, the MM\_SCF method is applicable in most of the basins (Fig. S8). The ME\_SCF method also slightly enhances the spatial performance of some dataset (Fig. 9a). The Noah\_SCF method, which accounts for the complex influence of underlying surface characteristics on SCF, has spatial performance comparable to MM\_SCF and ME\_SCF. This indicates that surface characteristics have a limited impact on spatial SCF accuracy. In contrast to the parameterization above, the aggressive MJ\_SCF approach with a 2-cm SD threshold to define the complete SCF (Table 1), reduces the spatial performance of all datasets, particularly in JRA55, which uses MJ\_SCF as its built-in method. Additionally, SCF obtained using the



MJ\_SCF method for all reanalysis datasets have large positive biases (Fig. S7), further reflecting its inapplicability. Orsolini et al. (2019) found that JRA55 performs well in SD simulation due to assimilating SD data from Chinese ground observation stations. When adopting a more appropriate method to transform SD into SCF, the bias of JRA55 significantly decreased, and the SS value increases from 0.57 to 0.81, comparable to the best-performing CFSR (Fig. 9a). This apparent improvement confirms the importance of parameterization to JRA55 SCF accuracy. Apart from JRA55, optimizing parameterization does not significantly alter the spatial performance ranking of the eight reanalysis datasets. For example, the SS values for MERRA2, ERA5, and ERA5L using the optimal MM\_SCF method are still lower than those for CFSR using the poorest MJ\_SCF method. This indirectly highlights the primary role of snowfall and temperature forcing inputs with respect to SCF simulations.

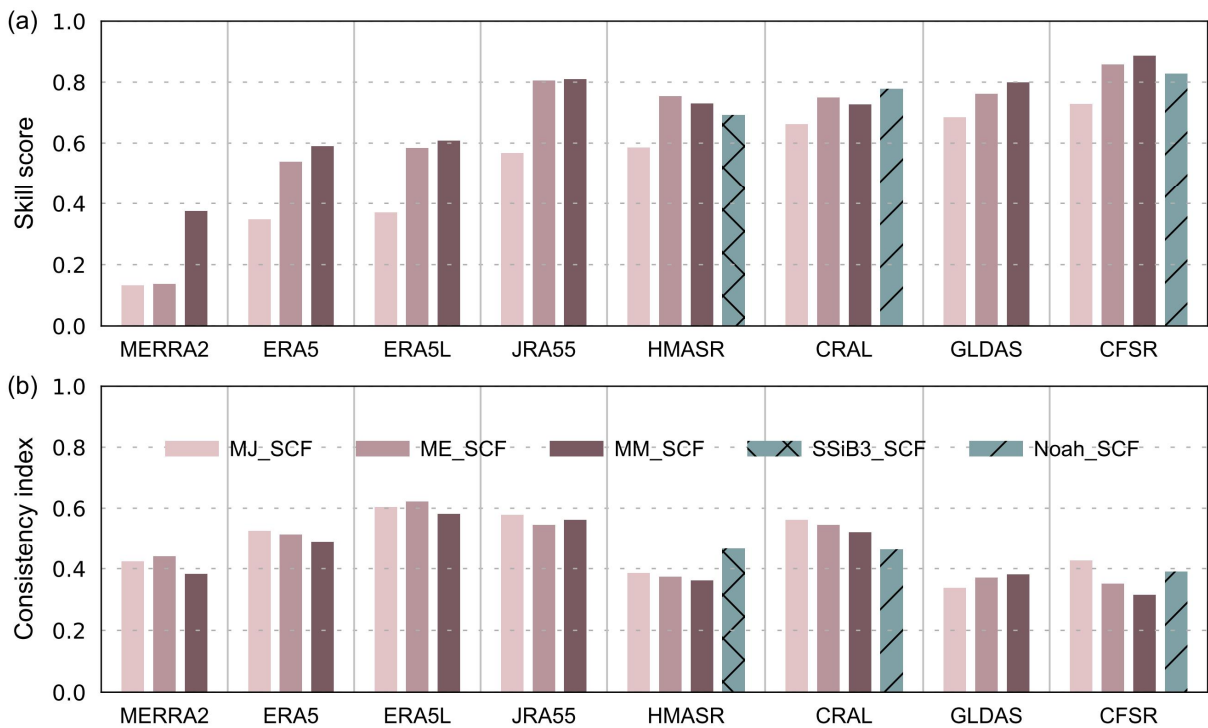


**Figure 9: SS (a) and CI (b) values of SCF for all reanalysis datasets calculated offline using the MM\_SCF, MJ\_SCF, and ME\_SCF parameterization methods. The green bars represent the built-in parameterization methods for HMASR, CRAL, and CFSR.**

### 3.3 Combination of reanalysis dataset for SCF optimization

Combining datasets can improve SCF accuracy, as evidenced by the SS and CI values of all  
530 combined datasets being higher than those of the single best-performing dataset (Fig. 10).  
However, SCF accuracy does not monotonically improve with the number of combined datasets.  
Spatially, the SS value improves when transitioning from CFSR alone to a combination with  
GLDAS and HMASR, but declines when more datasets are combined (Fig. 10a). This appears  
reasonable because CFSR, GLDAS, and HMASR have excellent accuracy in simulating SCF  
535 spatial variability, but adding poorly performing datasets (e.g., MERRA2 and JRA55)  
introduces more bias, resulting in a suboptimal outcome. Consequently, we concluded that a  
combination of CFSR, GLDAS, and HMASR is optimal for spatial SCF studies over the TP.  
Temporally, the highest CI value is achieved with the combination of more datasets, namely  
ERA5L, JRA55, HMASR, ERA5, GLDAS, and CRAL, which is different from the SS results  
540 (Fig. 10b). This is because reanalysis datasets generally have moderate SCF annual trend  
performance. Combining more datasets can help mitigate the shortcomings of individual  
datasets and improve the overall annual trend accuracy. In contrast to the optimal combination,  
the worst combination shows a monotonically and significantly improving performance for  
both spatial distribution and annual trends with increased number of combined datasets (Fig.  
545 10c and 10d).

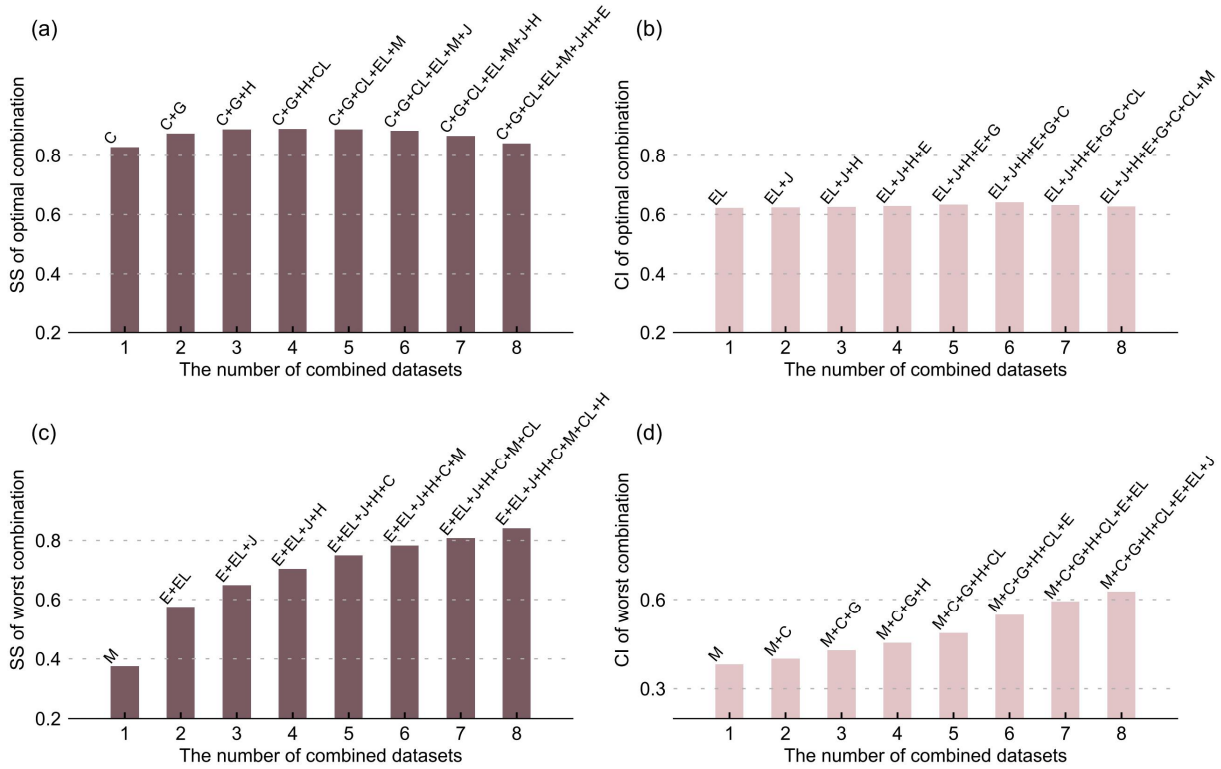


**Figure 10: (a) SS for optimal reanalysis dataset combinations across varying numbers of datasets. (b) As in (a) but for CI. (c) and (d) As in (a) and (b), but for the worst combinations. H: HMASR; M: MERRA2; E: ERA5; EL: ERA5L; J: JRA55; C: CFSR; CL: CRAL; G: GLDAS.**

550

## 4 Discussion

### 4.1 Effects of data assimilation, resolution, and LSM

Data assimilation is an effective approach for reducing snow model uncertainties and enhancing the capability to monitor seasonal snow changes (Andreadis and Lettenmaier, 2006; Sun et al., 2004). HMASR directly assimilates SCF data obtained from MODIS and Landsat satellites (Liu et al., 2021), which are processed using a spectral unmixing algorithm that has been found more accurate than the original band ratio methods (Stillinger et al., 2023). Under the same meteorological input fields as MERRA2, the data assimilation in HMASR corrects the widespread SCF underestimation and erroneous trends in the southwestern TP exhibited by MERRA2, enhancing the spatiotemporal simulation performance of HMASR. In contrast, lowest SS and CI values in SCF spatiotemporal simulations for MERRA2 may be partly related to its lack of SCF data assimilation. JRA55 and CFSR assimilate SD data and show good

560

simulation performance in SD and SWE (Bian et al., 2019; Orsolini et al., 2019). However, the  
565 process of converting SD to SCF in JRA55 introduces additional errors, limiting the impact of  
SD assimilation on SCF spatial simulation accuracy. In contrast, CFSR employs a more  
reasonable SCF parameterization, resulting in significantly higher spatial simulation  
performance compared to JRA55. This indirectly highlights the influence of parameterization  
methods on SCF simulation in JRA55.

570 The spatial resolution of reanalysis datasets and the choice of LSM may also affect the  
accuracy of SCF simulations. Lei et al. (2023) pointed out that reanalysis datasets characterized  
by finer spatial resolutions exhibit better consistency with in situ measurements of SD over the  
TP; e.g., ERA5L outperforms ERA5 and MERRA2. Sun et al. (2023) evaluated the ability of  
different LSMs to simulate SD in China based on station observation data and found that the  
575 community Noah LSM with multi-parameterization options (Noah-MP model) provided the  
best overall performance. In our study, the fine spatial resolution version of GLDAS generates  
better SCF simulations than the coarse spatial resolution version for both spatial distribution  
and annual trend (Fig. S1). Additionally, compared to the CLSM and VIC models, GLDAS  
simulations using the Noah model show better SCF performance at a  $1^\circ \times 1^\circ$  resolution. This  
580 indicates the non-negligible impact of model resolution and LSM choice on SCF simulation  
accuracy. However, SCF products with different spatial resolutions and LSMs are available  
only in GLDAS. Therefore, this study cannot conclusively state that the impact of spatial  
resolution and LSM on SCF accuracy is universal.

## 4.2 Limitations

585 This study focused primarily on the impact of snowfall and temperature factors in snow models,  
as well as the choice of SCF parameterization, on the performance of reanalysis datasets in  
simulating SCF over the TP. However, other model parameters related to precipitation and  
temperature, such as the precipitation gradient used to describe precipitation variations at  
different elevations, and the critical temperature used to distinguish rain from snow, are equally  
590 vital to snow simulations (Zhang et al., 2015). Furthermore, snow, being a suspended substance,

is susceptible to sublimation. It is estimated that blowing snow sublimation accounts for ~30% of global surface sublimation (Déry and Yau, 2002). The TP is perpetually influenced by the westerly jet stream, and processes such as blowing snow sublimation may be significant under windy and arid conditions. However, most LSMs used in reanalysis datasets do not consider blowing snow (Mortimer et al., 2020), and deficiencies in their model structures may also affect the accuracy of SCF simulations.

## 5. Conclusions

This study evaluates the ability and attributed the biases of eight widely used reanalysis datasets to simulate spatiotemporal variations in SCF over the TP based on SPIReS covering the period WYs 2001–2017. The results indicate that CRAL, GLDAS, and HMASR agree best with SPIReS in TP-averaged SCF and SS values all exceeding 0.7. CFSR, despite overestimating SCF, has the highest SS value due to good correlation with SPIReS and a high STDR value. These four datasets perform well spatially. In contrast, ERA5, ERA5L, and JRA55 generally overestimate SCF, while MERRA2 consistently underestimates it, leading to poor spatial performance. Overall, the reanalysis datasets exhibit moderate accuracy in annual trend analysis. ERA5L, JRA55, and ERA5 have relatively good temporal performance, with significant correlation in trend time series and better CI values in trend spatial consistency. GLDAS and CFSR perform poorly in trend representation. While MERRA2 has the worst performance in both spatial distribution and annual trend.

Snowfall and temperature significantly impact SCF bias. ERA5, ERA5L, and JRA55 overestimate SCF due to overestimated snowfall and underestimated temperature. Temperature-related physical processes have a more significant impact on SCF bias and its seasonal variations in these datasets. The poor trend performance in GLDAS and CFSR is due to inconsistent between temperature and snowfall trends compared to TPMFD trends. Meteorological factor errors impact the poor spatiotemporal performance of MERRA2. Additionally, the overestimation of SCF in JRA55 is also linked to aggressive parameterization. Except for JRA55, parameterization optimization improves SCF but does not significantly alter

the spatial performance ranking of the eight reanalysis datasets. To improve SCF accuracy, combining datasets is an effective method. A three-member combined of CFSR, GLDAS, and HMASR is optimal for the study of SCF spatial scales, while the combination of ERA5L, JRA55, HMASR, ERA5, GLDAS, and CRAL is optimal for the study of annual trends.

These findings are crucial for selecting the most suitable reanalysis SCF datasets and gaining deeper insights into SCF variations and their controlling mechanisms on the TP. Reducing uncertainties within reanalysis SCF datasets stands as a pivotal stride toward refining climate models and prediction systems. Considering the significant impact of precipitation and temperature bias, acquiring more precise meteorological forcing data is essential to further enhance the accuracy of reanalysis SCF simulations. Simultaneously, selecting more appropriate parameterization methods specific to reanalysis data models will contribute to improving dataset reliability. Optimizing simulations of snow cover on the TP will provide critical support for future climate change research and response strategies.

### **Conflicts of interest**

The authors declared that they have no conflicts of interest to this work. We declare that we do not have any commercial or associative interest that represents a conflict of interest in connection with the work submitted.

### **Data Availability Statement**

The SPIReS product used in this work is publicly available from <http://ftp.snow.ucsb.edu>. The TPMFD dataset are obtained from the National Tibetan Plateau Science Data Center (TPDC; <https://cstr.cn/18406.11.Atmos.tpd.300398>). All the reanalysis data are also acquired online: HMASR is obtained from on National Snow and Ice Data Center (NSIDC; <https://doi.org/10.5067/HNAUGJQXSCVU>). ERA5 and ERA5L data are downloaded from the Copernicus Climate Change Service Climate Data Store (CDS; <https://doi.org/10.24381>).

JRA55 and CFSR is downloaded from the NSF NCAR Research Data Archive (RDA; <https://rda.ucar.edu>). CRAL is obtained from the National Meteorological Information Center (CMA Meteorological Data Centre; <https://data.cma.cn/en>). MERRA2 and GLDAS-2.1 data is obtained from the NASA Goddard Earth Sciences Data and Information Service Center (GES DISC; <https://disc.gsfc.nasa.gov/>).

## Acknowledgments

This research was supported by the National Science Fund for Distinguished Young Scholars (42025102), the Natural Science Foundation of Gansu province, China (21ZDKA0017), the National Natural Science Foundation of China (42375068, 42075061, and 42301142) and “Double First Class” Special Guidance Project of Lanzhou University (561120205).

## References

- Adler, R. F., Huffman, G. J., Chang, A., Ferraro, R., Xie, P.-P., Janowiak, J., Rudolf, B., Schneider, U., Curtis, S., Bolvin, D., Gruber, A., Susskind, J., Arkin, P., and Nelkin, E.: The Version-2 Global Precipitation Climatology Project (GPCP) monthly precipitation analysis (1979–present), *J. Hydrometeorol.*, 4, 1147–1167, [https://doi.org/10.1175/1525-7541\(2003\)004<1147:TVGPCP>2.0.CO;2](https://doi.org/10.1175/1525-7541(2003)004<1147:TVGPCP>2.0.CO;2), 2003.
- Andreadis, K. M. and Lettenmaier, D. P.: Assimilating remotely sensed snow observations into a macroscale hydrology model, *Adv. Water Resour.*, 29, 872–886, <https://doi.org/10.1016/j.advwatres.2005.08.004>, 2006.
- Bair, E. H., Stilling, T., and Dozier, J.: Snow Property Inversion from Remote Sensing (SPIRES): a generalized multispectral unmixing approach with examples from MODIS and Landsat 8 OLI, *IEEE Trans. Geosci. Remote Sens.*, 59, 7270–7284, <https://doi.org/10.1109/TGRS.2020.3040328>, 2021.
- Bian, Q., Xu, Z., Zhao, L., Zhang, Y.-F., Zheng, H., Shi, C., Zhang, S., Xie, C., and Yang, Z.-L.: Evaluation and intercomparison of multiple snow water equivalent products over the Tibetan Plateau, *J. Hydrometeorol.*, 20, 2043–2055, <https://doi.org/10.1175/JHM-D-19-0011.1>, 2019.
- Brown, R. D. and Mote, P. W.: The response of Northern Hemisphere snow cover to a changing climate\*, *J. Clim.*, 22, 2124–2145, <https://doi.org/10.1175/2008JCLI2665.1>, 2009.

- Cao, B., Gruber, S., Zheng, D., and Li, X.: The ERA5-Land soil temperature bias in permafrost regions, *The Cryosphere*, 14, 2581–2595, <https://doi.org/10.5194/tc-14-2581-2020>, 2020.
- 670 Danielson, J. J. and Gesch, D. B.: Global multi-resolution terrain elevation data 2010 (GMTED2010), <https://doi.org/10.3133/ofr20111073>, 2011.
- de Rosnay, P., Balsamo, G., Albergel, C., Muñoz-Sabater, J., and Isaksen, L.: Initialisation of land surface variables for numerical weather prediction, *Surv. Geophys.*, 35, 607–621, <https://doi.org/10.1007/s10712-012-9207-x>, 2014.
- 675 Deng, H., Pepin, N. C., and Chen, Y.: Changes of snowfall under warming in the Tibetan Plateau, *J. Geophys. Res. Atmos.*, 122, 7323–7341, <https://doi.org/10.1002/2017JD026524>, 2017.
- Déry, S. J. and Yau, M. K.: Large-scale mass balance effects of blowing snow and surface sublimation, *J. Geophys. Res. Atmos.*, 107, ACL 8-1-ACL 8-17, <https://doi.org/10.1029/2001JD001251>, 2002.
- Ding, B., Yang, K., Qin, J., Wang, L., Chen, Y., and He, X.: The dependence of precipitation types on surface elevation and meteorological conditions and its parameterization, *J. Hydrol.*, 513, 154–163, <https://doi.org/10.1016/j.jhydrol.2014.03.038>, 2014.
- 680 Dozier, J., Painter, T. H., Rittger, K., and Frew, J. E.: Time–space continuity of daily maps of fractional snow cover and albedo from MODIS, *Adv. Water Resour.*, 31, 1515–1526, <https://doi.org/10.1016/j.advwatres.2008.08.011>, 2008.
- 685 Dutra, E., Kotlarski, S., Viterbo, P., Balsamo, G., Miranda, P. M. A., Schär, C., Bissolli, P., and Jonas, T.: Snow cover sensitivity to horizontal resolution, parameterizations, and atmospheric forcing in a land surface model, *J. Geophys. Res. Atmos.*, 116, <https://doi.org/10.1029/2011JD016061>, 2011.
- Ek, M. B., Mitchell, K. E., Lin, Y., Rogers, E., Grunmann, P., Koren, V., Gayno, G., and Tarpley, J. D.: Implementation of Noah land surface model advances in the National Centers for Environmental Prediction operational mesoscale Eta model, *J. Geophys. Res. Atmos.*, 108, 2002JD003296, <https://doi.org/10.1029/2002JD003296>, 2003.
- 690 Fujiwara, M., Wright, J. S., Manney, G. L., Gray, L. J., Anstey, J., Birner, T., Davis, S., Gerber, E. P., Harvey, V. L., Hegglin, M. I., Homeyer, C. R., Knox, J. A., Krüger, K., Lambert, A., Long, C. S., Martineau, P., Molod, A., Monge-Sanz, B. M., Santee, M. L., Tegtmeier, S., Chabrillat, S., Tan, D. G. H., Jackson, D. R., Polavarapu, S., Compo, G. P., Dragani, R., Ebisuzaki, W., Harada, Y., Kobayashi, C., McCarty, W., Onogi, K., Pawson,
- 695



- S., Simmons, A., Wargan, K., Whitaker, J. S., and Zou, C.-Z.: Introduction to the SPARC Reanalysis Intercomparison Project (S-RIP) and overview of the reanalysis systems, *Atmos. Chem. Phys.*, 17, 1417–1452, <https://doi.org/10.5194/acp-17-1417-2017>, 2017.
- 700 Gelaro, R., McCarty, W., Suárez, M. J., Todling, R., Molod, A., Takacs, L., Randles, C. A., Darmenov, A., Bosilovich, M. G., Reichle, R., Wargan, K., Coy, L., Cullather, R., Draper, C., Akella, S., Buchard, V., Conaty, A., Silva, A. M. da, Gu, W., Kim, G.-K., Koster, R., Lucchesi, R., Merkova, D., Nielsen, J. E., Partyka, G., Pawson, S., Putman, W., Rienecker, M., Schubert, S. D., Sienkiewicz, M., and Zhao, B.: The Modern-Era Retrospective analysis for Research and Applications, version 2 (MERRA-2), *J. Clim.*, 30, 5419–5454, <https://doi.org/10.1175/JCLI-D-16-0758.1>, 2017.
- 705 Hall, D. K., Riggs, G. A., Salomonson, V. V., DiGirolamo, N. E., and Bayr, K. J.: MODIS snow-cover products, *Remote Sens. Environ.*, 83, 181–194, [https://doi.org/10.1016/S0034-4257\(02\)00095-0](https://doi.org/10.1016/S0034-4257(02)00095-0), 2002.
- Helfrich, S. R., McNamara, D., Ramsay, B. H., Baldwin, T., and Kasheta, T.: Enhancements to, and forthcoming developments in the Interactive Multisensor Snow and Ice Mapping System (IMS), *Hydrol. Processes*, 21, 1576–1586, <https://doi.org/10.1002/hyp.6720>, 2007.
- 710 Hernández-Henríquez, M. A., Déry, S. J., and Derksen, C.: Polar amplification and elevation-dependence in trends of Northern Hemisphere snow cover extent, 1971–2014, *Environ. Res. Lett.*, 10, 044010, <https://doi.org/10.1088/1748-9326/10/4/044010>, 2015.
- Hersbach, H., Bell, B., Berrisford, P., Hirahara, S., Horányi, A., Muñoz-Sabater, J., Nicolas, J., Peubey, C., Radu, R., Schepers, D., Simmons, A., Soci, C., Abdalla, S., Abellan, X., Balsamo, G., Bechtold, P., Biavati, G., 715 Bidlot, J., Bonavita, M., Chiara, G., Dahlgren, P., Dee, D., Diamantakis, M., Dragani, R., Flemming, J., Forbes, R., Fuentes, M., Geer, A., Haimberger, L., Healy, S., Hogan, R. J., Hólm, E., Janisková, M., Keeley, S., Laloyaux, P., Lopez, P., Lupu, C., Radnoti, G., Rosnay, P., Rozum, I., Vamborg, F., Villaume, S., and Thépaut, J.: The ERA5 global reanalysis, *Q. J. R. Meteorolog. Soc.*, 146, 1999–2049, <https://doi.org/10.1002/qj.3803>, 2020.
- 720 Huang, J., Zhou, X., Wu, G., Xu, X., Zhao, Q., Liu, Y., Duan, A., Xie, Y., Ma, Y., Zhao, P., Yang, S., Yang, K., Yang, H., Bian, J., Fu, Y., Ge, J., Liu, Y., Wu, Q., Yu, H., Wang, B., Bao, Q., and Qie, K.: Global climate impacts of land - surface and atmospheric processes over the Tibetan Plateau, *Rev. Geophys.*, 61, e2022RG000771, <https://doi.org/10.1029/2022RG000771>, 2023.

- Huffman, G. J., Adler, R. F., Morrissey, M. M., Bolvin, D. T., Curtis, S., Joyce, R., McGavock, B., and Susskind, J.: Global precipitation at one-degree daily resolution from multisatellite observations, *J. Hydrometeorol.*, 2, 36–50, [https://doi.org/10.1175/1525-7541\(2001\)002<0036:GPAODD>2.0.CO;2](https://doi.org/10.1175/1525-7541(2001)002<0036:GPAODD>2.0.CO;2), 2001.
- Immerzeel, W. W., Van Beek, L. P. H., and Bierkens, M. F. P.: Climate change will affect the Asian water towers, *Science*, 328, 1382–1385, <https://doi.org/10.1126/science.1183188>, 2010.
- Jiang, Y., Chen, F., Gao, Y., He, C., Barlage, M., and Huang, W.: Assessment of uncertainty sources in snow cover simulation in the Tibetan Plateau, *J. Geophys. Res. Atmos.*, 125, <https://doi.org/10.1029/2020JD032674>, 2020.
- Jiang, Y., Yang, K., Qi, Y., Zhou, X., He, J., Lu, H., Li, X., Chen, Y., Li, X., Zhou, B., Mantimin, A., Shao, C., Ma, X., Tian, J., and Zhou, J.: TPhIPr: a long-term (1979–2020) high-accuracy precipitation dataset (1 / 30°, daily) for the Third Pole region based on high-resolution atmospheric modeling and dense observations, *Earth Syst. Sci. Data*, 15, 621–638, <https://doi.org/10.5194/essd-15-621-2023>, 2023.
- Kitoh, A. and Arakawa, O.: Reduction in the east–west contrast in water budget over the Tibetan Plateau under a future climate, *Hydrol. Res. Lett.*, 10, 113–118, <https://doi.org/10.3178/hrl.10.113>, 2016.
- Kobayashi, S., Ota, Y., Harada, Y., Ebata, A., Moriya, M., Onoda, H., Onogi, K., Kamahori, H., Kobayashi, C., Endo, H., Miyaoka, K., and Takahashi, K.: The JRA-55 Reanalysis: General Specifications and Basic Characteristics, *J. Meteorolog. Soc. Jpn.*, 93, 5–48, <https://doi.org/10.2151/jmsj.2015-001>, 2015.
- Koster, R. D., Suarez, M. J., Ducharne, A., Stieglitz, M., and Kumar, P.: A catchment-based approach to modeling land surface processes in a general circulation model: 1. Model structure, *J. Geophys. Res. Atmos.*, 105, 24809–24822, <https://doi.org/10.1029/2000JD900327>, 2000.
- Lehner, B., Verdin, K., and Jarvis, A.: New Global Hydrography Derived From Spaceborne Elevation Data, *EoS Transactions*, 89, 93–94, <https://doi.org/10.1029/2008EO100001>, 2008.
- Lei, Y., Pan, J., Xiong, C., Jiang, L., and Shi, J.: Snow depth and snow cover over the Tibetan Plateau observed from space in against ERA5: matters of scale, *Clim. Dyn.*, 60, 1523–1541, <https://doi.org/10.1007/s00382-022-06376-0>, 2023.
- Li, Q., Yang, T., and Li, L.: Evaluation of snow depth and snow cover represented by multiple datasets over the Tianshan Mountains: Remote sensing, reanalysis, and simulation, *Int. J. Climatol.*, 42, 4223–4239, <https://doi.org/10.1002/joc.7459>, 2022.
- Liang, X., Jiang, L., Pan, Y., Shi, C., Liu, Z., and Zhou, Z.: A 10-Yr global land surface reanalysis interim dataset

- (CRA-Interim/Land): Implementation and preliminary evaluation, *J. Meteorolog. Res.*, 34, 101–116, <https://doi.org/10.1007/s13351-020-9083-0>, 2020.
- 755 Lin, H. and Wu, Z.: Contribution of the autumn Tibetan Plateau snow cover to seasonal prediction of North American winter temperature, *J. Clim.*, 24, 2801–2813, <https://doi.org/10.1175/2010JCLI3889.1>, 2011.
- Liu, Y., Fang, Y., Li, D., and Margulis, S. A.: How well do global snow products characterize snow storage in High Mountain Asia?, *Geophys. Res. Lett.*, 49, <https://doi.org/10.1029/2022GL100082>, 2022.
- Liu, Y., Fang, Y., and Margulis, S. A.: Spatiotemporal distribution of seasonal snow water equivalent in High Mountain Asia from an 18-year Landsat–MODIS era snow reanalysis dataset, *The Cryosphere*, 15, 5261–  
760 5280, <https://doi.org/10.5194/tc-15-5261-2021>, 2021.
- Liu, Z., Jiang, L., Shi, C., Zhang, T., Zhou, Z., Liao, J., Yao, S., Liu, J., Wang, M., Wang, H., Liang, X., Zhang, Z., Yao, Y., Zhu, T., Chen, Z., Xu, W., Cao, L., Jiang, H., and Hu, K.: CRA-40/Atmosphere—the first-generation Chinese atmospheric reanalysis (1979–2018): System description and performance evaluation, *J. Meteorolog. Res.*, 37, 1–19, <https://doi.org/10.1007/s13351-023-2086-x>, 2023.
- 765 Luo, J., Chen, H., and Zhou, B.: Comparison of Snowfall Variations over China Identified from Different Snowfall/Rainfall Discrimination Methods, *J. Meteorol. Res.*, 34, 1114–1128, <https://doi.org/10.1007/s13351-020-0004-z>, 2020.
- Lyu, M., Wen, M., and Wu, Z.: Possible contribution of the inter-annual Tibetan Plateau snow cover variation to the Madden-Julian oscillation convection variability, *Int. J. Climatol.*, 38, 3787–3800,   
770 <https://doi.org/10.1002/joc.5533>, 2018.
- Ma, Y., Ma, W., Zhong, L., Hu, Z., Li, M., Zhu, Z., Han, C., Wang, B., and Liu, X.: Monitoring and Modeling the Tibetan Plateau’s climate system and its impact on East Asia, *Sci. Rep.*, 7, 44574, <https://doi.org/10.1038/srep44574>, 2017.
- Meng, J., Yang, R., Wei, H., Ek, M., Gayno, G., Xie, P., and Mitchell, K.: The land surface analysis in the NCEP  
775 climate forecast system reanalysis, *J. Hydrometeorol.*, 13, 1621–1630, <https://doi.org/10.1175/JHM-D-11-090.1>, 2012.
- Mortimer, C., Mudryk, L., Derksen, C., Luoju, K., Brown, R., Kelly, R., and Tedesco, M.: Evaluation of long-term Northern Hemisphere snow water equivalent products, *The Cryosphere*, 14, 1579–1594, <https://doi.org/10.5194/tc-14-1579-2020>, 2020.

- 780 Mudryk, L. R., Derksen, C., Kushner, P. J., and Brown, R.: Characterization of Northern Hemisphere snow water equivalent datasets, 1981–2010, *J. Clim.*, 28, 8037–8051, <https://doi.org/10.1175/JCLI-D-15-0229.1>, 2015.
- Muñoz-Sabater, J., Dutra, E., Agustí-Panareda, A., Albergel, C., Arduini, G., Balsamo, G., Boussetta, S., Choulga, M., Harrigan, S., Hersbach, H., Martens, B., Miralles, D. G., Piles, M., Rodríguez-Fernández, N. J., Zsoter, E., Buontempo, C., and Thépaut, J.-N.: ERA5-Land: a state-of-the-art global reanalysis dataset for land applications, *Earth Syst. Sci. Data*, 13, 4349–4383, <https://doi.org/10.5194/essd-13-4349-2021>, 2021.
- 785 Onogi, K., Tsutsui, J., Koide, H., Sakamoto, M., Kobayashi, S., Hatsushika, H., Matsumoto, T., Yamazaki, N., Kamahori, H., Takahashi, K., Kadokura, S., Wada, K., Kato, K., Oyama, R., Ose, T., Mannoji, N., and Taira, R.: The JRA-25 reanalysis, *J. Meteorolog. Soc. Jpn.*, 85, 369–432, <https://doi.org/10.2151/jmsj.85.369>, 2007.
- Orsolini, Y., Wegmann, M., Dutra, E., Liu, B., Balsamo, G., Yang, K., De Rosnay, P., Zhu, C., Wang, W., Senan, R., and Arduini, G.: Evaluation of snow depth and snow cover over the Tibetan Plateau in global reanalyses using in situ and satellite remote sensing observations, *The Cryosphere*, 13, 2221–2239, <https://doi.org/10.5194/tc-13-2221-2019>, 2019.
- 790 Painter, T. H., Rittger, K., McKenzie, C., Slaughter, P., Davis, R. E., and Dozier, J.: Retrieval of subpixel snow covered area, grain size, and albedo from MODIS, *Remote Sens. Environ.*, 113, 868–879, <https://doi.org/10.1016/j.rse.2009.01.001>, 2009.
- 795 Pu, W., Cui, J., Wu, D., Shi, T., Chen, Y., Xing, Y., Zhou, Y., and Wang, X.: Unprecedented snow darkening and melting in New Zealand due to 2019–2020 Australian wildfires, *Fundam. Res.*, 1, 224–231, <https://doi.org/10.1016/j.fmre.2021.04.001>, 2021.
- Qiu, J.: China: The third pole, *Nature*, 454, 393–396, <https://doi.org/10.1038/454393a>, 2008.
- 800 Reichle, R. H., Draper, C. S., Liu, Q., Girotto, M., Mahanama, S. P. P., Koster, R. D., and Lannoy, G. J. M. D.: Assessment of MERRA-2 Land Surface Hydrology Estimates, *J. Clim.*, 30, 2937–2960, <https://doi.org/10.1175/JCLI-D-16-0720.1>, 2017.
- Rodell, M., Houser, P. R., Jambor, U., Gottschalck, J., Mitchell, K., Meng, C.-J., Arsenault, K., Cosgrove, B., Radakovich, J., Bosilovich, M., Entin, J. K., Walker, J. P., Lohmann, D., and Toll, D.: The global land data assimilation system, *Bull. Am. Meteorol. Soc.*, 85, 381–394, <https://doi.org/10.1175/BAMS-85-3-381>, 2004.
- 805 Saha, S., Moorthi, S., Pan, H.-L., Wu, X., Wang, J., Nadiga, S., Tripp, P., Kistler, R., Woollen, J., Behringer, D., Liu, H., Stokes, D., Grumbine, R., Gayno, G., Wang, J., Hou, Y.-T., Chuang, H., Juang, H.-M. H., Sela, J.,

Iredell, M., Treadon, R., Kleist, D., Van Delst, P., Keyser, D., Derber, J., Ek, M., Meng, J., Wei, H., Yang, R., Lord, S., Van Den Dool, H., Kumar, A., Wang, W., Long, C., Chelliah, M., Xue, Y., Huang, B., Schemm, J.-K., Ebisuzaki, W., Lin, R., Xie, P., Chen, M., Zhou, S., Higgins, W., Zou, C.-Z., Liu, Q., Chen, Y., Han, Y., Cucurull, L., Reynolds, R. W., Rutledge, G., and Goldberg, M.: The NCEP climate forecast system reanalysis, *Bull. Am. Meteorol. Soc.*, 91, 1015–1058, <https://doi.org/10.1175/2010BAMS3001.1>, 2010.

810

Saha, S., Moorthi, S., Wu, X., Wang, J., Nadiga, S., Tripp, P., Behringer, D., Hou, Y.-T., Chuang, H., Iredell, M., Ek, M., Meng, J., Yang, R., Mendez, M. P., Van Den Dool, H., Zhang, Q., Wang, W., Chen, M., and Becker, E.: The NCEP climate forecast system version 2, *J. Clim.*, 27, 2185–2208, <https://doi.org/10.1175/JCLI-D-12-00823.1>, 2014.

815

Sato, N., Sellers, P. J., Randall, D. A., Schneider, E. K., Shukla, J., Kinter, J. L., Hou, Y.-T., and Albertazzi, E.: Effects of implementing the Simple Biosphere Model in a general circulation model, *J. Atmos. Sci.*, 46, 2757–2782, [https://doi.org/10.1175/1520-0469\(1989\)046<2757:EOITSB>2.0.CO;2](https://doi.org/10.1175/1520-0469(1989)046<2757:EOITSB>2.0.CO;2), 1989.

820

Sellers, P. J., Mintz, Y., Sud, Y. C., and Dalcher, A.: A Simple Biosphere Model (SIB) for use within general circulation models, *J. Atmos. Sci.*, 43, 505–531, [https://doi.org/10.1175/1520-0469\(1986\)043<0505:ASBMFU>2.0.CO;2](https://doi.org/10.1175/1520-0469(1986)043<0505:ASBMFU>2.0.CO;2), 1986.

Serquet, G., Marty, C., Dulex, J.-P., and Rebetez, M.: Seasonal trends and temperature dependence of the snowfall/precipitation-day ratio in Switzerland, *Geophys. Res. Lett.*, 38, <https://doi.org/10.1029/2011GL046976>, 2011.

825

Sheffield, J., Goteti, G., and Wood, E. F.: Development of a 50-Year High-Resolution Global Dataset of Meteorological Forcings for Land Surface Modeling, *J. Clim.*, 19, 3088–3111, <https://doi.org/10.1175/JCLI3790.1>, 2006.

Stillinger, T., Rittger, K., Raleigh, M. S., Michell, A., Davis, R. E., and Bair, E. H.: Landsat, MODIS, and VIIRS snow cover mapping algorithm performance as validated by airborne lidar datasets, *The Cryosphere*, 17, 567–590, <https://doi.org/10.5194/tc-17-567-2023>, 2023.

830

Sun, C., Walker, J. P., and Houser, P. R.: A methodology for snow data assimilation in a land surface model, *J. Geophys. Res. Atmos.*, 109, 2003JD003765, <https://doi.org/10.1029/2003JD003765>, 2004.

Sun, S. and Xue, Y.: Implementing a new snow scheme in Simplified Simple Biosphere Model, *Adv. Atmos. Sci.*, 18, 335–354, <https://doi.org/10.1007/BF02919314>, 2001.

835

- Sun, S., Shi, C., Liang, X., Zhang, S., Gu, J., Han, S., Jiang, H., Xu, B., Yu, Q., Liang, Y., and Deng, S.: The Evaluation of Snow Depth Simulated by Different Land Surface Models in China Based on Station Observations, *Sustainability*, 15, 11284, <https://doi.org/10.3390/su151411284>, 2023.
- 840 Thackeray, C. W., Fletcher, C. G., Mudryk, L. R., and Derksen, C.: Quantifying the Uncertainty in Historical and Future Simulations of Northern Hemisphere Spring Snow Cover, *J. Clim.*, 29, 8647–8663, <https://doi.org/10.1175/JCLI-D-16-0341.1>, 2016.
- Vorkauf, M., Marty, C., Kahmen, A., and Hiltbrunner, E.: Past and future snowmelt trends in the Swiss Alps: the role of temperature and snowpack, *Clim. Change*, 165, 44, <https://doi.org/10.1007/s10584-021-03027-x>, 2021.
- 845 Wang, A. and Zeng, X.: Evaluation of multireanalysis products with in situ observations over the Tibetan Plateau, *J. Geophys. Res. Atmospheres*, 117, D05102, <https://doi.org/10.1029/2011JD016553>, 2012.
- Wegmann, M., Orsolini, Y., Dutra, E., Bulygina, O., Sterin, A., and Brönnimann, S.: Eurasian snow depth in long-term climate reanalyses, *The Cryosphere*, 11, 923–935, <https://doi.org/10.5194/tc-11-923-2017>, 2017.
- 850 Xie, P. and Arkin, P. A.: Global precipitation: A 17-year monthly analysis based on gauge observations, satellite estimates, and numerical model Outputs, *Bull. Am. Meteorol. Soc.*, 78, 2539–2558, [https://doi.org/10.1175/1520-0477\(1997\)078<2539:GPAYMA>2.0.CO;2](https://doi.org/10.1175/1520-0477(1997)078<2539:GPAYMA>2.0.CO;2), 1997.
- Xie, P., Chen, M., Yang, S., Yatagai, A., Hayasaka, T., Fukushima, Y., and Liu, C.: A gauge-based analysis of daily precipitation over East Asia, *J. Hydrometeorol.*, 8, 607–626, <https://doi.org/10.1175/JHM583.1>, 2007.
- Xu, W., Ma, L., Ma, M., Zhang, H., and Yuan, W.: Spatial–temporal variability of snow cover and depth in the 855 Qinghai–Tibetan Plateau, *J. Clim.*, 30, 1521–1533, <https://doi.org/10.1175/JCLI-D-15-0732.1>, 2017.
- Xu, X., Lu, C., Shi, X., and Gao, S.: World water tower: An atmospheric perspective, *Geophys. Res. Lett.*, 35, L20815, <https://doi.org/10.1029/2008GL035867>, 2008.
- Xue, Y., Sun, S., Kahan, D. S., and Jiao, Y.: Impact of parameterizations in snow physics and interface processes on the simulation of snow cover and runoff at several cold region sites, *J. Geophys. Res. Atmos.*, 108, 2002JD003174, <https://doi.org/10.1029/2002JD003174>, 2003.
- 860 Yang, D., Ding, M., Dou, T., Han, W., Liu, W., Zhang, J., Du, Z., and Xiao, C.: On the Differences in Precipitation Type Between the Arctic, Antarctica and Tibetan Plateau, *Front. Earth Sci.*, 9, <https://doi.org/10.3389/feart.2021.607487>, 2021.

- 865 Yang, K., Jiang, Z., Tang, W., He, J., Shao, C., Zhou, X., Lu, H., Chen, Y., Li, X., and Shi, J.: A high-resolution near-surface meteorological forcing dataset for the Third Pole region (TPMFD, 1979-2022), <https://doi.org/10.11888/Atmos.tpsc.300398>, 2023.
- Yang, M., Wang, X., Pang, G., Wan, G., and Liu, Z.: The Tibetan Plateau cryosphere: Observations and model simulations for current status and recent changes, *Earth Sci. Rev.*, 190, 353–369, <https://doi.org/10.1016/j.earscirev.2018.12.018>, 2019.
- 870 Yao, T., Thompson, L., Yang, W., Yu, W., Gao, Y., Guo, X., Yang, X., Duan, K., Zhao, H., Xu, B., Pu, J., Lu, A., Xiang, Y., Kattel, D. B., and Joswiak, D.: Different glacier status with atmospheric circulations in Tibetan Plateau and surroundings, *Nat. Clim. Change*, 2, 663–667, <https://doi.org/10.1038/nclimate1580>, 2012.
- Yao, T., Xue, Y., Chen, D., Chen, F., Thompson, L., Cui, P., Koike, T., Lau, W. K.-M., Lettenmaier, D., Mosbrugger, V., Zhang, R., Xu, B., Dozier, J., Gillespie, T., Gu, Y., Kang, S., Piao, S., Sugimoto, S., Ueno, K., Wang, L., 875 Wang, W., Zhang, F., Sheng, Y., Guo, W., Ailikun, Yang, X., Ma, Y., Shen, S. S. P., Su, Z., Chen, F., Liang, S., Liu, Y., Singh, V. P., Yang, K., Yang, D., Zhao, X., Qian, Y., Zhang, Y., and Li, Q.: Recent Third Pole's Rapid Warming Accompanies Cryospheric Melt and Water Cycle Intensification and Interactions between Monsoon and Environment: Multidisciplinary Approach with Observations, Modeling, and Analysis, *Bull. Am. Meteorol. Soc.*, 100, 423–444, <https://doi.org/10.1175/BAMS-D-17-0057.1>, 2019.
- 880 You, Q., Wu, F., Wang, H., Jiang, Z., Pepin, N., and Kang, S.: Projected changes in snow water equivalent over the Tibetan Plateau under global warming of 1.5° and 2°C, *J. Clim.*, 33, 5141–5154, <https://doi.org/10.1175/JCLI-D-19-0719.1>, 2020a.
- You, Q., Wu, T., Shen, L., Pepin, N., Zhang, L., Jiang, Z., Wu, Z., Kang, S., and AghaKouchak, A.: Review of snow cover variation over the Tibetan Plateau and its influence on the broad climate system, *Earth Sci. Rev.*, 885 201, 103043, <https://doi.org/10.1016/j.earscirev.2019.103043>, 2020b.
- Yu, L., Zhang, S., Bu, K., Yang, J., Yan, F., and Chang, L.: A review on snow data sets, *Scientia Geographica Sinica*, 33, 878–883, <https://doi.org/10.13249/j.cnki.sgs.2013.07.878>, 2013.
- Zhang, F., Zhang, H., Hagen, S. C., Ye, M., Wang, D., Gui, D., Zeng, C., Tian, L., and Liu, J.: Snow cover and runoff modelling in a high mountain catchment with scarce data: effects of temperature and precipitation 890 parameters, *Hydrol. Processes*, 29, 52–65, <https://doi.org/10.1002/hyp.10125>, 2015.
- Zhang, H., Zhang, F., Che, T., Yan, W., and Ye, M.: Investigating the ability of multiple reanalysis datasets to

simulate snow depth variability over mainland China from 1981 to 2018, *J. Clim.*, 34, 9957–9972, <https://doi.org/10.1175/JCLI-D-20-0804.1>, 2021.

895 Zhang, H., Immerzeel, W. W., Zhang, F., De Kok, R. J., Chen, D., and Yan, W.: Snow cover persistence reverses the altitudinal patterns of warming above and below 5000 m on the Tibetan Plateau, *Sci. Total Environ.*, 803, 149889, <https://doi.org/10.1016/j.scitotenv.2021.149889>, 2022.

Zhang, T.: Influence of the seasonal snow cover on the ground thermal regime: An overview, *Rev. Geophys.*, 43, RG4002, <https://doi.org/10.1029/2004RG000157>, 2005.

900 Zhou, X., Yang, K., Ouyang, L., Wang, Y., Jiang, Y., Li, X., Chen, D., and Prein, A.: Added value of kilometer-scale modeling over the third pole region: a CORDEX-CPTP pilot study, *Clim. Dyn.*, 57, 1673–1687, <https://doi.org/10.1007/s00382-021-05653-8>, 2021.

Zhu, X., Wu, T., Li, R., Wang, S., Hu, G., Wang, W., Qin, Y., and Yang, S.: Characteristics of the ratios of snow, rain and sleet to precipitation on the Qinghai-Tibet Plateau during 1961–2014, *Quat. Int.*, 444, 137–150, <https://doi.org/10.1016/j.quaint.2016.07.030>, 2017.

905